JGR Solid Earth

RESEARCH ARTICLE
10.1029/2021JB022734

Special Section:
Ophiolites and Oceanic Lithosphere, with a focus on the Samail ophiolite in Oman

A Reference Section Through Fast-Spread Lower Oceanic Crust, Wadi Gideah, Samail Ophiolite (Sultanate of Oman): Whole Rock Geochemistry

Dieter Garbe-Schönberg[1,2], Jürgen Koepke[3], Samuel Müller[1], Dominik Mock[3], and Tim Müller[3]

[1]Institute of Geosciences, Kiel University, Kiel, Germany, [2]Department of Physics and Earth Sciences, Jacobs University Bremen, Bremen, Germany, [3]Institute of Mineralogy, Leibniz University Hannover, Hannover, Germany

Key Points:

- A coherent compositional transect through fossil oceanic crust for major and 38 trace elements, compositions for Samail oceanic crust
- Systematic but contrasting compositional trends correlate with stratigraphic depth over 6,500 m of plutonic crust
- A discontinuity at ~3,525 m above Moho separates lower cumulate gabbros crystallized in situ from upper gabbros fractionated in melt lens

Supporting Information:

Supporting Information may be found in the online version of this article.

Correspondence to:

D. Garbe-Schönberg,
dieter.garbe-schoenberg@ifg.uni-kiel.de

Citation:

Garbe-Schönberg, D., Koepke, J., Müller, S., Mock, D., & Müller, T. (2022). A reference section through fast-spread lower oceanic crust, Wadi Gideah, Samail Ophiolite (Sultanate of Oman): Whole rock geochemistry. *Journal of Geophysical Research: Solid Earth*, *127*, e2021JB022734. https://doi.org/10.1029/2021JB022734

Received 30 JUN 2021
Accepted 1 JUN 2022

Author Contributions:

Conceptualization: Dieter Garbe-Schönberg, Jürgen Koepke
Data curation: Dieter Garbe-Schönberg

Abstract Due to its inaccessibility, no complete and coherent data set exists for the composition of modern fast-spreading oceanic crust. We sampled outcrops through 6,500 m of fossil oceanic crust in the Oman Ophiolite (Wadi Gideah Transect) that is regarded as best analogue of fast-spreading crust on land. Here we report a complete set of whole-rock major and trace element data displaying systematic and contrasting compositional trends in lower and upper gabbros being correlated with stratigraphic depth. A significant discontinuity in crystallization regime is observed at ~3,525 m above the mantle-crust boundary: gabbros below ~3,525 m have in general very low incompatible element mass fractions which develop upwards in a barely noticeable way to more differentiated compositions while Mg# decreases. More pronounced trends indicating progressive fractionation of ascending melts can be observed for incompatible elements and their element ratios as a consequence of in situ crystallization. Locally, more variable compositions within narrow depth intervals testify for advanced differentiation in situ within individual sills. Gabbros above ~3,525 m become significantly more evolved and show considerable variations in composition. Fractional crystallization and mixing processes in a transient axial melt lens control the composition of isotropic "varitextured" gabbros and sheeted dike basalts where fractionation of high field strength elemental ratios is minor. New average compositions of fast-spread (paleo) oceanic crust are reported for major and 38 trace elements. Comparison with new data from Wadi Khafifah close to Wadi Gideah suggests robustness of crustal accretion processes in both space and time.

Plain Language Summary Oceanic crust covers more than two-thirds of Earth's surface but, due to limited accessibility, no single coherent compositional profile that would allow for understanding the processes how oceanic crust is formed has been obtained up to now. We sampled a transect through 6.5 km of fossil lower oceanic crust of the Samail ophiolite (Sultanate of Oman, Wadi Gideah) that is regarded as best analogue of fast-spreading oceanic crust on land, and analyzed all samples with a wide selection of techniques. Here, we present whole rock data and see systematic compositional trends correlating with stratigraphic depth. Distribution trends of incompatible trace elements suggest that lower, layered gabbros are made of cumulus crystals that crystallize in situ, separating from the ascending parental magma. We also find gabbros with variable compositions at intermediate depth intervals that could originate from melts crystallizing and differentiating in sills. In contrast, compositions of upper non-layered gabbros above ~3,525 m above the mantle-crust boundary are controlled by fractional crystallization and mixing processes in transient melt lenses. New average compositions of (paleo) oceanic crust are reported for major and 38 trace elements. Comparison with new data from Wadi Khafifah close to Wadi Gideah suggests robustness of accretion processes in both space and time.

1. Introduction

Oceanic crust covers more than two-thirds of Earth's surface and 90% of Earth's volcanism is associated with the formation of oceanic lithosphere along a 60,000 km network of oceanic spreading ridges. The formation of oceanic crust is one of the dominant processes in the chemical differentiation and physical evolution of our planet exerting primary control on the transfer of material, heat, and volatiles from Earth's interior to its crust, oceans, and atmosphere. Knowledge of the composition of oceanic crust is a prerequisite for the calculation of their fluxes and for testing models of crustal accretion and magma differentiation at oceanic spreading ridges.

Formal analysis: Dieter Garbe-Schönberg, Samuel Müller, Dominik Mock
Funding acquisition: Dieter Garbe-Schönberg, Jürgen Koepke
Investigation: Dieter Garbe-Schönberg, Samuel Müller, Dominik Mock, Tim Müller
Methodology: Dieter Garbe-Schönberg, Samuel Müller, Tim Müller
Project Administration: Dieter Garbe-Schönberg, Jürgen Koepke
Resources: Dieter Garbe-Schönberg
Supervision: Dieter Garbe-Schönberg
Validation: Dieter Garbe-Schönberg
Writing – original draft: Dieter Garbe-Schönberg, Dominik Mock
Writing – review & editing: Jürgen Koepke, Samuel Müller, Dominik Mock

Oceanic crust formed at fast-spreading ridges as in the southeastern Pacific exhibits a relatively uniform seismic stratigraphy and bathymetry and is regarded as layered and relatively homogeneous (e.g., Anonymous, 1972; Canales et al., 2003). First described in the Penrose model (Anonymous, 1972) it is composed of basalt lava, diabase sheeted dikes, and gabbros overlying mantle peridotites (from top to bottom; see Figures 1 and 2). Consequently, our understanding of crustal accretion processes and related geochemical cycles and fluxes can be extrapolated to a significant portion of Earth's surface with some confidence. Previous efforts of the Ocean Drilling Program (ODP) and International Ocean Discovery Program (IODP) to sample modern fast-spreading oceanic crust include Hole 504B on the southern flank of the Costa Rica Rift that penetrated 1.8 km into ~6.9 Ma Pacific Ocean igneous basement but recovered only lavas and dikes (Alt et al., 1996). Drill hole 1256D into the basement of the Guatemala basin that was formed by the East Pacific Rise (EPR) ~15 Ma ago successfully cored a 1,507 m long section of the upper oceanic crust reaching the underlying uppermost gabbros (Teagle et al., 2012; Wilson et al., 2006). In addition to these IODP drillings, two other prominent locations of fast-spread oceanic crust formed at the EPR in the Equatorial Eastern Pacific expose deeper crustal parts due to ridge tectonism: Hess Deep and Pito Deep. Instead of drilling coherent profiles, ship-based in situ sampling using a remotely operated vehicle was performed very locally as a function of depth at both Hess Deep and Pito Deep, and very short ODP and IODP drill cores were obtained at Hess Deep enabling the construction of "pseudo"-sections of oceanic crust, as summarized in Coogan (2014), and references therein. However, these "sections" cannot serve as a representative "reference" for deep fast-spreading oceanic crust for the following reasons: (a) the data sets are incomplete; (b) faults related to ridge tectonics cause many problems in correlating sampling depths; (c) due to the special tectonic situation with propagating rifts at these sites it is not clear whether the local magmatism is representative for fast-spreading crust in general; and (d) there is no upward stratigraphic continuation into the volcanic sequence. Consequently, a coherent "reference" profile through modern fast-spreading oceanic crust is still missing and will not be obtained in the near future.

As an alternative to sampling the modern oceanic crust, a reference profile through fast-spreading crust can be obtained by sampling an ophiolite section. However, most ophiolites either lack a coherent stratigraphy or are of subduction-related setting (e.g., Shervais, 2001). Only the Samail ophiolite in the Sultanate of Oman appears suitable for such an attempt based on results from previous studies performed over the last decades (see Nicolas & Poliakov, 2001 for details and below) which also led to its status as the type location for oceanic crust as hypothesized in the Penrose model (Anonymous, 1972). Especially the southern part of the ophiolite is least influenced by subduction processes when compared to the northern part and closely resembles fast-spreading oceanic crust. Unfortunately, most sample collections and analytical data sets from previous work before the 2020s were not coherent enough to qualify as a proper reference profile for fast-spreading oceanic crust. Due to this deficiency, most models for the accretion of fast-spreading crust have not been tested against natural samples (Gillis et al., 2014; Teagle et al., 2012). Only very recently, VanTongeren et al. (2021), presented a comprehensive study based on a sampling transect through lower paleo-oceanic crust in the Wadi Khafifah section of the Samail ophiolite (Oman) and developed a new model where the lower oceanic crust is accreted entirely by the injection of small sills of primitive melts.

We sampled a complete crustal transect in the Samail ophiolite from mantle rocks to pillow basalts from outcrops along Wadi Gideah in the Wadi Tayin massif and followed a multi-method analytical approach for studying petrographical and petrological, mineral chemical (Koepke et al., 2022; Müller, 2016), micro-structural (Mock, Ildefonse, et al., 2021), and whole rock geochemical properties (this study) of this sample suite in great detail as a basis for testing models of accretion of fast-spreading oceanic crust. This transect is comprehensive in terms of completeness and coherence of samples from all crustal sections but has recently been further complemented by the ICDP (International Continental Scientific Drilling Program) Oman Drilling Project (OmanDP, https://www.omandrilling.ac.uk/) with drill holes GT1 and GT2 in Wadi Gideah (Kelemen et al., 2020) sampling lower sections of the plutonic crust in situ and in very high resolution. Here, we present new data for major and trace element compositions along the Wadi Gideah transect and discuss the implications of our data for accretion processes of the lower oceanic crust. Special attention will be paid to new data from the Wadi Khafifah transect (VanTongeren et al., 2021) which is in only 10 km distance from our transect.

1.1. The Samail Ophiolite as a Representative Fragment of Oceanic Lithosphere

The Samail ophiolite—a ~400 km long mountain chain of oceanic lithosphere obducted onto the Arabic continental margin during the Cretaceous—is regarded as the best example of fast-spreading (ancient) oceanic crust on

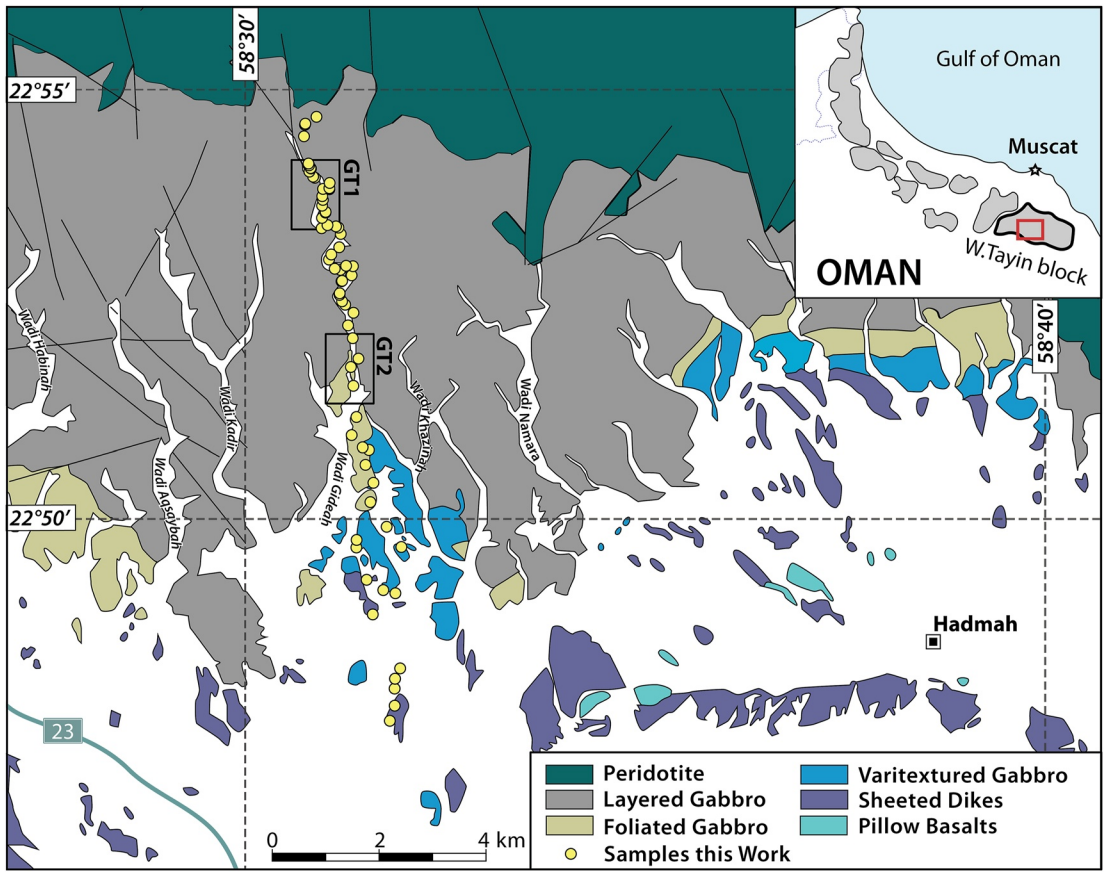

Figure 1. Sampling locations (yellow dots) of the coherent transect along the NNW-SSE trending Wadi Gideah in the southern part of the Wadi Tayin massif (Samail ophiolite). Black frames mark the positions of drill holes GT1 and GT2 of the ICDP Oman Drilling Project. Geological map modified after Peters et al. (2005) and Müller (2016). See also Supporting Information Data Set S1 for exact sampling positions.

land (e.g., Nicolas et al., 2000). Initial work on the Samail ophiolite started with a US mapping project performed in 1978–1979. In the course of that project, a sample suite was collected through the entire ophiolite in the Ibra area of the Wadi Tayin massif. Samples were studied for O, Sr, Nd, Pb isotopes (Chen & Pallister, 1981; Gregory & Taylor, 1981; McCulloch et al., 1981) and for rare earth elements (REE) (Pallister & Knight, 1981; major elements and other trace elements were not included), and a petrological profile based on mineral compositions was established (Pallister & Hopson, 1981; but only a few data were presented). The obtained results represented the state-of-the-art at that time, for example, the evaluation of a model of km-thick magma chambers under the ridges filled with pure melt (Cann, 1974). The "ophiolite model" for the composition and structure of the oceanic crust was developed (Coleman, 1981; Hopson et al., 1981; Pallister & Hopson, 1981), and an early model for the alteration of oceanic crust via hydrothermal circulation was presented (Gregory & Taylor, 1981; McCulloch et al., 1981). Moreover, the first radiometric ages for the Samail ophiolite were obtained (McCulloch et al., 1981; Tilton et al., 1981). Thirty years later, our understanding of the geodynamics of ocean ridges has increased tremendously due to ship-based science: substantial differences between fast- and slow-spreading ridges have been established (e.g., Dick et al., 2006); a small melt lens at the top of the gabbro sequence has been discovered (e.g., Detrick et al., 1987); there is an enhanced understanding of the process of crustal accretion; numerous black smokers and hydrothermal systems have been discovered. Continued research on the Samail ophiolite led to for example, the discovery of primary ridge tectonics influencing the magmatic regime (Boudier et al., 1988), and the discovery of a secondary magmatic phase related to the initial stage of subduction (e.g., Alabaster et al., 1982). Zircon dating revealed that the paleo-crust was formed ~95 Ma ago under fast-spreading conditions with a half-spreading rate of 50–100 mm/yr (Rioux et al., 2012, 2013).

Geochemical investigations (e.g., Koepke et al., 2009; Pearce et al., 1981; Yamasaki et al., 2006) suggest a polygenetic origin for the Samail ophiolite. A first phase produced the so-called V1 lavas and gabbroic rocks

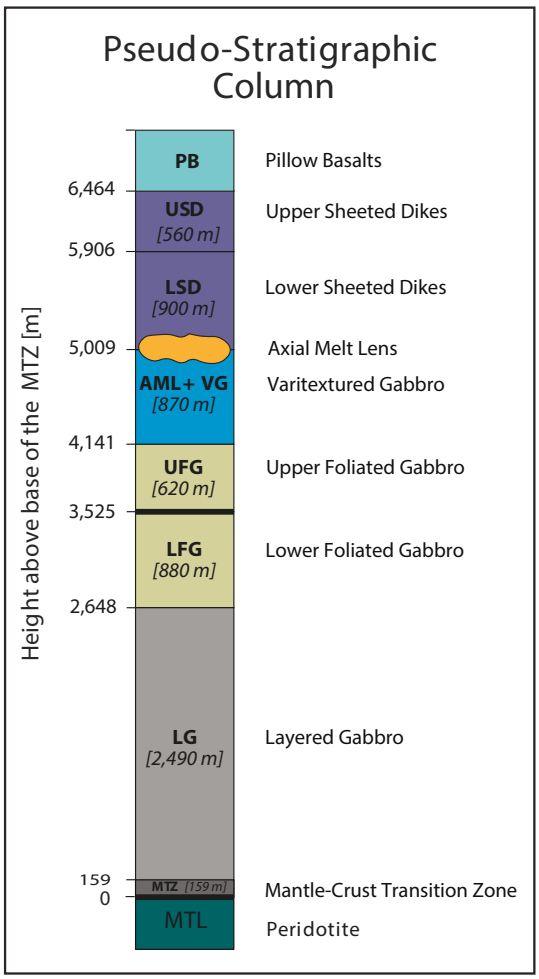

Figure 2. Pseudo-stratigraphic column of the lower crust in Wadi Gideah with definition of individual sections from Mantle-Crust Transition Zone (MTZ) at the base up to Upper Sheeted Dikes at the top (after Koepke et al., 2022; Mock et al., 2021) and their boundaries in (m) height above base of the MTZ. Also given is the thickness of individual units.

similar to "mid-ocean ridge basalts" (MORB) and related plutonics formed at a typical fast-spreading oceanic spreading center but with some influence from subduction initiation. This rock sequence is typical for the Wadi Gideah in the southern part of the Samail ophiolite. A second magmatic phase related to flux melting of mantle produced more "wet" lavas, depleted in incompatible trace elements, with affinities to typical lavas erupted during subduction zone initiation. These later so-called V2 lavas are related to characteristic plutonics in the crust, as crosscutting highly depleted gabbronorites and wehrlites. The second magmatic stage is much more voluminous in the northern blocks of the ophiolite than in the southern part (e.g., Goodenough et al., 2014; MacLeod et al., 2013). In order to constrain magmatic processes during the initial MORB-type V1-stage of the crustal formation we have chosen Wadi Gideah in the southernmost Wadi Tayin block for collecting our samples (Figure 1) where magmatic rocks related to the V2 volcanism are nearly absent.

The parental basaltic melts for the first magmatic stage (V1) are modeled to have elevated water contents of 0.4%–0.8% due to their formation in a subduction-influenced setting (Koepke et al., 2021; MacLeod et al., 2013; Müller et al., 2017). In spite of the inferred location of the ophiolite in a region of subduction zone initiation, the following observations related to the first magmatic phase demonstrate a close similarity with the modern, fast-spreading EPR: (a) a continuous layered crustal structure with a typical crustal thickness of ~6 km, including a coherent plutonic section consisting of typical layered gabbros with a layering parallel to the crust/mantle boundary; (b) absence of typical "amagmatic" spreading that is common at slow-spreading ridges; (c) a very narrow range of zircon crystallization ages across the width of the ophiolite (max ~ 100 km) sampled normal to the ridge direction; (d) spinel Cr/Al versus Mg# ratios that overlap those for peridotites from modern ridges; and (e) a well-developed sheeted dike sequence, orientated perpendicular to the Moho (Koepke et al., 2022).

1.2. Crustal Accretion at Fast-Spreading Oceanic Ridges

Prominent conceptual models for the formation of lower plutonic crust at fast-spreading ridges are (a) the "Gabbro-Glacier" model (e.g., Henstock et al., 1993; Phipps Morgan & Chen, 1993; Quick & Denlinger, 1993) where all of the crystallization occurs in a shallow axial melt lens (AML), and where the accumulated crystal residues subside along the walls of the magma chamber to build the lower crust; (b) the "Sheeted Sills" model (e.g., Bédard et al., 1988; Kelemen & Aharanov, 1998; Kelemen et al., 1997; Korenaga & Kelemen, 1997), where significant parts of the plutonic crust are formed by in situ crystallization from sill injection of gabbroic mushes in the deep crust. This model was recently extended to the "Full Sheeted Sills" model where primitive magmas from the mantle are injected as sills throughout the lower crust, crystallize in situ, and release evolved magmas to replenish the upper gabbros (VanTongeren et al., 2021); (c) hybrid accretion models which either combine a "Gabbro Glacier" subsiding from the AML with randomly intruding sills at depth crystallizing in situ (e.g., Boudier et al., 1996; Maclennan et al., 2004; Natland & Dick, 2009), or combine a crystal mush-dominated vertical melt flow in the upper third with in situ sill crystallization in the lower two thirds of the plutonic sequence (Mock, Ildefonse, et al., 2021). The two end-member models—"Gabbro Glacier" and "Sheeted Sills"—have profoundly different implications for the properties of the lower crust, including its composition, the distribution of melt, the extent of deformation, the thermal history, and the geometry, temperature, and intensity of hydrothermal fluid-rock exchange (for details see Teagle et al., 2012).

The "Gabbro Glacier" model postulates that the differentiation of primitive MORB melt is all taking place within the AML below the sheeted dikes and, consequently, the lower crust forms as cumulate from settling crystal mushes and should have constant and homogeneous composition in terms of for example, Mg# (molar

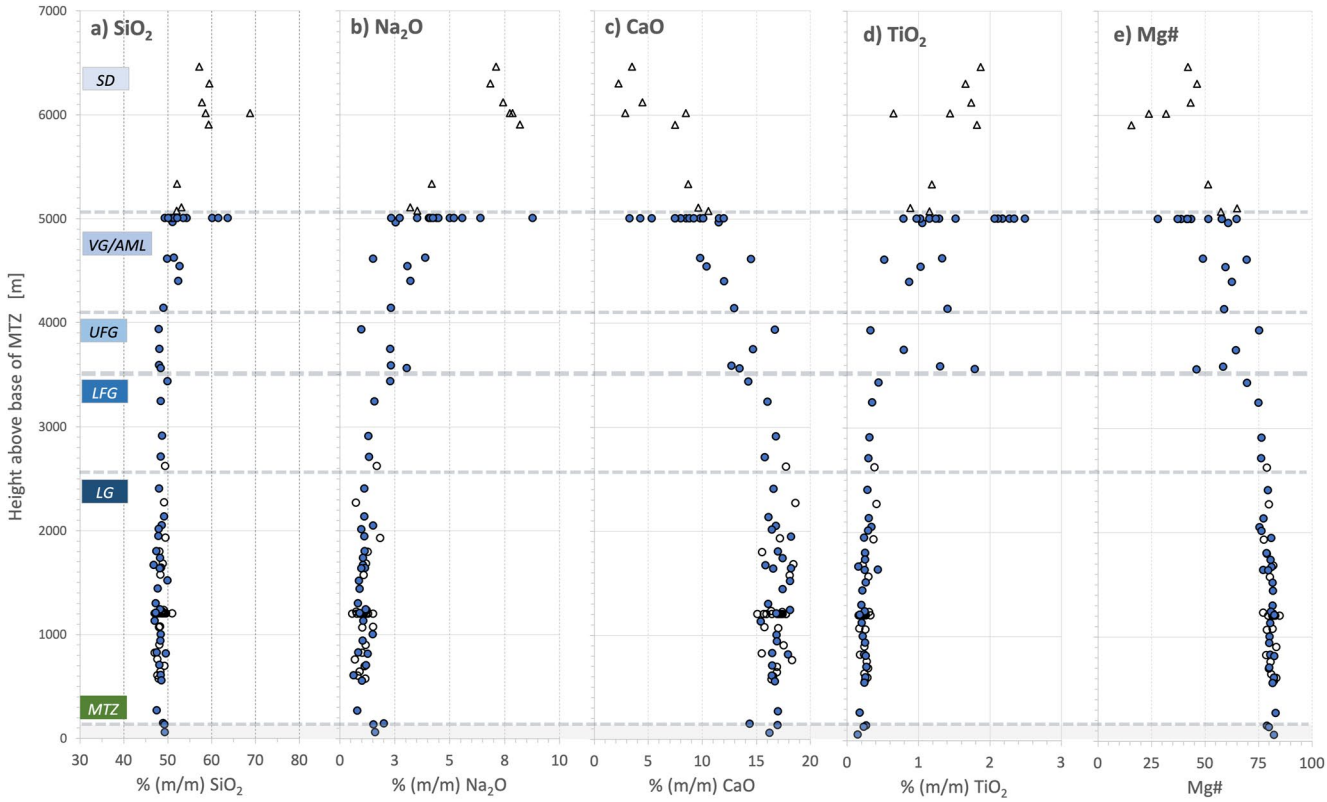

Figure 3. Compositional transects through Wadi Gideah plutonic crust as a function of stratigraphic height over the base of the MTZ: (a) SiO_2, (b) Na_2O, (c) CaO, (d) TiO_2, and (e) Mg#. *Open triangles*: sheeted dikes (*SD*); *filled circles*: "normal," relatively fresh gabbro and gabbroic rocks; *open circles*: gabbros influenced by hydrothermal fault zones. *VG/AML*: varitextured gabbros and samples from the frozen axial melt lens; *UFG*, *LFG*: upper and lower foliated gabbros; *LG*: layered gabbros; *MTZ*: mantle-crust transition zone.

MgO/(MgO + FeO) × 100) in clinopyroxene and olivine cores and in bulk rock chemistry; accretion is top-down. On the other hand, the "Sheeted Sills" models build on individual injection and differentiation of sills in the deep crust during ascent of primitive MORB melt, with a significant compositional change in the upper gabbros representing the "compositional conjugate" of the lower cumulate gabbros (Kelemen et al., 1997). Accretion can be seen here as a bottom-up process. Results obtained so far in the lower crust of fast-spreading oceanic crust are inconsistent: a profile sampled from outcrops in the Wadi Abyad in the Samail ophiolite revealed constant Mg# with depth (MacLeod & Yaouancq, 2000: Figure 3), while IODP drilling at Hess Deep into the upper and lower gabbros revealed a zoned lower crust with evolved gabbros at the top and primitive gabbros at the base of the crust (Gillis et al., 2014). New results from Koepke et al. (2022) and Müller et al. (2022) from the Wadi Gideah Transect show a trend of decreasing Mg# in olivine and An in plagioclase with increasing distance from the mantle-crust boundary.

Individual gabbro samples from modern oceans recovered by dredge surveys or seafloor sampling highlight the role of melt/rock interaction during formation of the lower crust (e.g., Lissenberg & Dick, 2008; Lissenberg et al., 2013). These studies touch on the important aspect of how melt is transported within the deep crust, in particular the importance of porous flow versus magmatic injection in dikes and sills, and then what is the fate of the evolved melts, whether they eventually lead to the formation of oceanic plagiogranites.

1.3. Geological Setting and Crustal Units of the Samail Ophiolite

The Wadi Gideah crosscuts the Wadi Tayin Block of the Samail ophiolite (e.g., Nicolas et al., 2000; Pallister & Hopson, 1981) in nearly N-S direction (Figure 1) and offers ideal conditions for sampling a continuous profile through the almost undisturbed plutonic section of ancient oceanic crust. A geological map can be found in Nicolas et al. (2000). Based on microstructural, textural, and petrological data Mock, Ildefonse, et al. (2021)

and Koepke et al. (2022) identified discrete lithological units of the lower crust in the Wadi Gideah reference profile which is followed here for consistency. Pillow basalts were not found in this Wadi. Basaltic to doleritic sheeted dikes (SD, ~1,500 m thickness, Figure 2) link the extrusives to underlying varitextured gabbros (VG) that are represented by isotropic, often hornblende and Fe-Ti-oxide bearing gabbros with patchy appearance, called "varitextured" due to their variable textures (Koepke et al., 2022). They are also known as "isotropic" or "upper" gabbro (MacLeod & Yaouancq, 2000; Pallister & Hopson, 1981). Some of the varitextured gabbros in the transect show a significant lineation (Mock, Ildefonse, et al., 2021) while others are isotropic. These rocks are only known from fast-spreading ridges where they are regarded as frozen fillings of the AML. The association of VG with crosscutting dikes of quartz diorites and tonalites, late trondhjemite, and basaltic dikes at the top of this transect is assumed to represent a frozen AML (Müller, 2017). The transition to the underlying relatively fine-grained foliated gabbros (FG) occurs at 4,138 m above the base of the mantle-crust transition zone (MTZ). The lineation is still present in the upper foliated gabbros (UFG), but abruptly decreases at 3,525 m above the base of the MTZ pronouncing the separation of the upper from the lower foliated gabbros (LFG). A significant grain size coarsening at ~2,648 m above the base of the MTZ marks the change from the FG unit to the layered cumulate gabbros (LG). The latter show an increase in fabric strength and the progressive return of a lineated fabric down section. Samples from the lowermost 159 m of the profile are ascribed to the MTZ.

2. Material and Methods

2.1. Outcrop Sampling

A total of 293 samples were collected during field work in 2010 (OM10), 2011 (OM11), 2012 (OM12), and 2015 (OM15) from outcrops along the Wadi Gideah. Sampling locations were projected on an idealized vertical transect through the ophiolitic crust dipping at an angle of 28°S (Pallister and Hopson, 1981), and the distance of each sample relative to the base of the MTZ was calculated and expressed as "Height above base of MTZ" in all tables and figures (see Koepke et al., 2022 for details). In the field, the MTZ can be more precisely located as a reference than the top of the sheeted dikes and pillow lavas representing the ancient seafloor for these rocks; those units are rarely preserved and occur only in discontinuous outcrops. From this sample suite, 116 representative samples with roughly equidistant sampling locations (average ~70 m projected distance between samples) have been selected for further processing and detailed geochemical study (Figure 1). However, it must be kept in mind that this sample series taken from outcrops is highly biased toward lithologies that are robust against intense weathering. Small occurrences of more primitive rock types like for example, wehrlites have probably been missed.

To avoid duplication and clustering of samples at certain depths in the transect, the number of samples was further reduced to a total of 108 samples comprising 9 samples from SD, 21 samples of the VG unit including 15 samples from one outcrop interpreted as a fossil axial melt lens (AML; Müller et al., 2017), 8 samples of the foliated gabbro unit (UFG and LFG), 41 samples of the layered gabbro unit (LG), and 3 samples from the MTZ (Figure 2). For the characterization of the crustal units and for a detailed petrography and petrology of the investigated samples see Koepke et al. (2022). Crosscutting veinlets and dikes have been excluded from this suite. All sample locations and petrographic classifications of samples are compiled in Supporting Information Data Set S1 (Garbe-Schönberg et al., 2022) and follow closely the classifications as reported in Koepke et al. (2022). Average sample size was in the decimeter range, always making sure that the local textural variability (e.g., grain size, modal layering) was entirely covered in that respective sample, and that enough material was available for subsampling for the different analytical techniques used here and in the other complementary studies (Koepke et al., 2022; Mock, Ildefonse, et al., 2021; Müller et al., 2022).

2.2. Sample Preparation and Analysis: A Comparison of Methods for Whole Rock Analysis

For bulk rock analysis, diamond saw-cut slabs avoiding weathered rock parts were disintegrated by a jaw crusher and a stainless-steel mortar at the Universities of Münster and Hannover, Germany. Rock fragments were then hand-picked and sonicated in a 50/50 (v/v) mixture of deionized water and ethanol. After drying, pulverization was done by agate oscillating disc milling until the powder passed a 74 μm sieve. Unfortunately, all OM12 samples have been contaminated with lead during preparation and data for Pb will not be reported for these samples.

Oceanic plutonic rocks may contain abundant accessory minerals like spinel, zircon, etc. that are extremely refractory during hot-plate multi-acid digestion, and even high-pressure PARR bomb digestion is not always able to completely dissolve these minerals. Hence, we conducted a comprehensive comparison of different sample preparation procedures and methods for the bulk analysis of plutonic rocks. While all samples were digested by (a) a standard table-top multi-acid procedure (Garbe-Schönberg, 1993), a sub-selection of 37 representative rocks covering all rock types from our sample suite was processed by (b) high-pressure multi-acid digestion using PARR bomb autoclaves with subsequent solution-based analysis; (c) pressed powder tablets after ultra-milling to nano-particulate powders with subsequent analysis by laser ablation–inductively coupled plasma–mass spectrometry (LA-ICP-MS) (Garbe-Schönberg & Müller, 2014); (d) glasses obtained from shock-melting using a strip-heater with subsequent analysis by LA-ICP-MS (Stoll et al., 2008); (e) glasses produced in pressure-sealed gold tubes (Botcharnikov et al., 2013) with subsequent analysis by LA-ICP-MS; (f) lithiumborate fused glass beads with subsequent analysis by WD-XRF, and compared to the initial analytical results after hot-plate multi-acid digestion. More details on those sample preparation steps and the analytical procedures are presented in the Supporting Information and in Tables S1 and S2.

The method comparison shows that hot plate multi-acid digestion cannot dissolve zircon completely giving too low mass fractions of Zr, Hf, Nb, Ta, and heavy rare earth elements (HREE) in the analyses of gabbro and more differentiated plutonic rocks. Interestingly, the deficiency of Zr in the analyses using multi-acid digestions begins at only 40 μg/g Zr in gabbro from our Wadi Gideah transect suggesting that a refractory Zr phase—presumably zircon as baddeleyite is unlikely to form at low oxygen fugacities—must be present in these rocks (Supporting Information Figure S1). Moreover, the incomplete dissolution of spinel (chromite) in ultramafic rocks from the MTZ manifests in low recoveries for Cr and Ni. Nevertheless, all other elements can be analyzed with excellent precision and accuracy from multi-acid digest solutions. The high-pressure multi-acid digestion with PARR autoclaves can be taken as a reference procedure giving precise and accurate results for almost all elements investigated here, but results for Cr, Ni, and Mo, Sb and Cs tend to be too high. Accurate results were also obtained from LA-ICP-MS analyses using nano-particulate pressed powder pellets and shock-melted glasses but, analyses with LA-ICP-MS in general have slightly worse analytical precision in the range of 1–3%RSD (1SD) when compared to solution-based analyses and show more deviation for transition metals (e.g., Cd, Pb, Zn, Mo) and volatiles (e.g., Sb). The shock-melted glasses produced with the strip heater were heterogeneous in composition and showed significant losses of volatiles (e.g., alkali metals, Mo, Sb, Pb, U) and strong contamination from the material of the heating strip (Ir, W, Pb at low sub-μg/g mass fractions). It was not possible to melt Mg-rich ultramafic rocks (e.g., serpentinite, harzburgite) nor differentiated rocks with elevated silica (e.g., granite) with this type of a strip-heater. Seven samples were processed to homogeneous glasses under high-pressure conditions avoiding the loss of volatiles. The composition of these glasses fit very well with data from high-pressure acid digestion, nano-particulate pellets, and strip-heater glasses but are low in Mo. Results obtained from WD-XRF analyses agreed well with data obtained from LA-ICP-MS measurements and high-pressure digestions but instrumental detection limits had been neglected as can be seen in for example, the systematically high recoveries for Ba and Zr at low concentrations <~50 μg/g (see Supporting Information Table S2 and Figure S1). After careful examination of all results obtained from the different procedures for sample preparation we decided to use the very precise and accurate results from multi-acid digestion for most elements but replaced data for refractory high field strength elements (HFSE: Zr, Hf, Nb, Ta), HREE (Y, Tb-Lu), and Th (and Cr, Ni in ultramafic rocks) by data from LA-ICP-MS analysis of nano-particulate pressed powder tablets. The latter data set showed excellent agreement with results obtained from high-pressure acid digestions and strip heater glasses but slightly worse analytical precision.

The complete compilation of all data from the method comparison experiments and more detailed descriptions of the analytical procedures used are in the Supporting Information S1. Here we give only brief summaries of analytical methods used for producing the final data set.

2.3. Analytical Procedures for Bulk Analysis

2.3.1. Major Elements by Inductively Coupled Plasma–Optical Emission Spectrometry (ICP-OES)

For the determination of major and minor element compositions multi-acid digest solutions were 10-fold diluted with 2% (v/v) subboiled nitric acid and spiked to 5 μg/g Y for internal standardization prior to analysis. A radial viewing simultaneous spectrometer (Ciros SOP, Spectro Analytical Instruments) was used under standard

operating conditions. Matrix-matched calibration was done with digest solutions of certified reference materials basalt BHVO-2, basalt BE-N, and granite AC-E. Accuracy was monitored with running digest solutions of basalt BIR-1, gabbro JGb-2, granite JG-2, andesite W-2, and peridotite PCC-1 as unknowns. Analytical precision was estimated from at least 10% duplicate measurements of samples and found to be better than 0.5%–1%. For silicon cannot be determined from multi-acid digestions with HF we calculated SiO_2 as the difference between 100% and the total of all major elements and loss-on-ignition. All major element data used in tables and figures are recalculated on anhydrous basis to 100% with total iron reported as FeO. Results for samples are compiled in Supporting Information Data Set S1.

2.3.2. Trace Elements by Liquid Sample Introduction ICP-MS

Data for all trace elements except HFSE (Zr, Hf, Nb, Ta), HREE and Y, and Th have been determined from acid digestion solutions by liquid sample introduction ICP-MS using both quadrupole-based instrumentation (7500cs and 7900, Agilent Technologies) and a high-resolution sector-field ICP-MS (Element XR, Thermo Scientific) operated under standard conditions with perfluoralkoxy micro-nebulization. Sample digest solutions were 10–20-fold diluted with 2% (v/v) subboiled nitric acid and spiked to 2.5 ng/g Be, In, Re for internal standardization using gravimetrically calibrated pipettes. Interferences from polyatomic ions of Ba and La on Eu, Gd were corrected with correction factors actually determined from synthetic solutions analyzed with every sample batch. A more detailed description of instrument calibration and data evaluation procedures is given in Garbe-Schönberg (1993). Laboratory procedural blanks, at least 10% sample duplicates, and international reference materials were analyzed with every sample batch. The analytical precision as estimated from the analysis of sample duplicates is typically better than 0.5–1%RSD (1SD) for all elements analyzed. All results for trace elements are reported in Supporting Information Data Set S1.

2.3.3. Trace Elements by LA-ICP-MS Using Nano-Particulate Powder Tablets

Data for HFSE (Zr, Hf, Nb, Ta), HREE and Y, and Th were taken from analyses using nano-particulate powder pellets (see Supporting Information S1 for detailed description). A 193 nm ArF excimer laser ablation system (GeoLasPro HD, Coherent) coupled to an Agilent 7500s or 8900 ICP-MS was used for all measurements. Samples as nano-particulate pressed powder tablets were loaded into a Zurich-type two volume laser ablation cell (LDHCLAC, Fricker et al., 2011) flushed with 1.0 L min^{-1} He as the carrier gas. Addition of 14 mL min^{-1} H_2 into the He carrier gas stream before entering the ablation cell led to an increase in sensitivity (typically >40 cps/1 µg/g La) and reduction of oxide formation to ~0.1% ThO/Th at robust plasma conditions with U/Th ≈ 1.05. Each measurement comprised data acquisition intervals of 20 s background, 40–60 s sample ablation, and 20 s washout monitoring. To reduce potential errors from surface contamination the first 5–10 s of each sample acquisition were discarded from data integration. The GLITTER software package was used for data reduction and setting integration windows in time-resolved data. External calibration was done with silicate glass NIST SRM612 using ^{48}Ca for internal standardization. A second matrix-matched calibration step was done in offline spreadsheet software using the international reference materials BIR-1G, BHVO-2G, BCR-2G, and MPI-DING glasses KL-2, StHs-60, GOR-128, and GOR-132. In addition, nano-particulate pressed powder tablets of JGb-1, JB-2a, BIR-1a, and BHVO-2 were used for checking accuracy of the results. All data were background corrected and represent averages of 3–5 spot analyses. The analytical precision as estimated from replicate analyses is typically better than 1–5%RSD (1SD) for all elements analyzed at concentrations >10× limit of detection. Results for international reference materials and all results for trace elements are reported in Supporting Information Data Set 1, and lower limits of detection are reported in Supporting Information Table S2. More details of the analytical procedure and results for reference materials that were analyzed in line with samples from the Wadi Gideah transect can be found in Garbe-Schönberg and Müller (2014).

3. Results and Discussion

All analytical results for the sample transect are tabulated in Supporting Information Data Set S1 and graphically displayed in Supporting Information S2 for convenience. The data presented here should be compared to, and interpreted in the context of, the companion papers by Mock, Ildefonse, et al. (2021) for microstructures, Koepke et al. (2022) for petrography and mineral chemistry, and Müller et al. (2022) for mineral chemistry and thermometry.

Based on microstructures of 68 gabbros from the Wadi Gideah transect, Mock et al. (2021) divided the gabbro sequence into two groups: the "lower gabbros" composed of the LG and LFG forming the lower 2/3 of the gabbro sequence, and the "upper gabbros" composed of the UFG and the varitextured gabbros corresponding to the frozen fillings of the AMLs. Upper and lower gabbros are divided by a narrow discontinuity at ~3,525 m above base of the MTZ. According to Mock et al. (2021), the dominant rock-forming process below this discontinuity was compaction, while the foliated and some varitextured gabbros above this discontinuity show a marked lineation produced by a flow of crystal-laden melts. Other varitextured gabbro show isotropic textures implying a formation by simple freezing of melt reservoirs. Building on this observation, Koepke et al. (2022) suggested on the basis of mineral trends and petrological modeling that the lower gabbros correspond more or less to pure compacted cumulus minerals crystallized from upwards moving parental MORB melts which mixed with replenished melts. On the other hand, the upper gabbros correspond to downward flowing differentiated melts or mushes originated from the AML, which mixed with upward moving differentiated melts originated from the lower gabbros. Based on very primitive relics in minerals from the varitextured gabbros Müller et al. (2022) showed that at least some of the AML reservoirs have been initially filled with primitive parental MORB melt, which was probably directly transported from the mantle to the AML. This explains some rather primitive compositions found in the AML horizon. In the following, we show that our results for bulk rock geochemistry are in full accord with findings of Mock et al. (2021), Koepke et al. (2022), and Müller et al. (2022).

While gabbros from the lowermost 3,525 m of this section are characterized by very low trace element mass fractions and in general only small changes in composition with height above the mantle-crust boundary, gabbros from the uppermost 1,280 m show significant increases in incompatible trace element concentration with increasing height. These findings are almost identical to results of VanTongeren et al. (2021) for the Wadi Khafifah Section 10 km to the West reporting 3,700 m and 1,500 m depth intervals for "lower" and "upper gabbros." One of the striking features of our transect in Wadi Gideah, however, is the development of compositional trends toward more evolved rock compositions with increasing distance from the MTZ. These trends are barely recognizable in the lower gabbros but statistically significant, and much more pronounced in the upper gabbros. In the Wadi Khafifah transect, no such trends are observed in the lower gabbro section (VanTongeren et al., 2021). Superimposed on the general trend especially in the lower gabbros are individual fractionation trends over short distances of the profile for example, at ~1,200 m, ~1,950 m, and 2,400–2,600 m above base of the MTZ (see Figures 3–5), and some samples with very primitive compositions have been found also in very high stratigraphic levels for example, in the frozen AML at 5,009 m above the base of the MTZ. These individual trends become even more visible in the mineral compositions of olivine, clinopyroxene, and plagioclase from the corresponding samples (see Koepke et al., 2022 for major elements, and Müller et al., 2022 for trace elements in minerals). Our observations will be discussed below in the context of sill injection as the dominant accretion process (see Section 3.1.2). The general compositional trends become obvious in almost all bulk compositional profiles for major and trace elements in both lower and upper gabbros but are very prominent in the distributions of highly incompatible elements like for example, Zr, La, or Th. Similar findings are reported for some incompatible elements in the Wadi Khafifah transect (VanTongeren et al., 2021). This general trend can also be seen in the corresponding minerals composition versus crustal depth plots in Figure 9 in Koepke et al. (2022) and in Müller et al. (2022).

3.1. Lower Gabbros

3.1.1. Mantle-Crust Transition Zone and Cumulate Layered Gabbros

The transect begins at the petrographic mantle/crust boundary. The base of the MTZ is defined as the sharp transition from harzburgites representing mantle rocks to the first coherent cumulate rocks. These MTZ rocks represent 159 m of the transect and consist of cumulate dunites, wehrlites, troctolites, and layered olivine gabbro transitioning into layered gabbros without any discontinuity (Koepke et al., 2022). The absence of cumulate dunite marks the beginning of the LG showing a typical modal layering on the cm to dm scale with alternating darker olivine-rich and lighter plagioclase-rich layers. This unit is ~2,490 m thick, with layering sub-parallel to the mantle/crust boundary. No plastic deformation has been observed in these rocks (Mock, Ildefonse, et al., 2021; Mock et al., 2020).

The distribution of many major elements is more or less homogeneous with no obvious trend up-section in LG but the lowermost LG samples are characterized by slightly more primitive compositions reaching Mg# 83 when

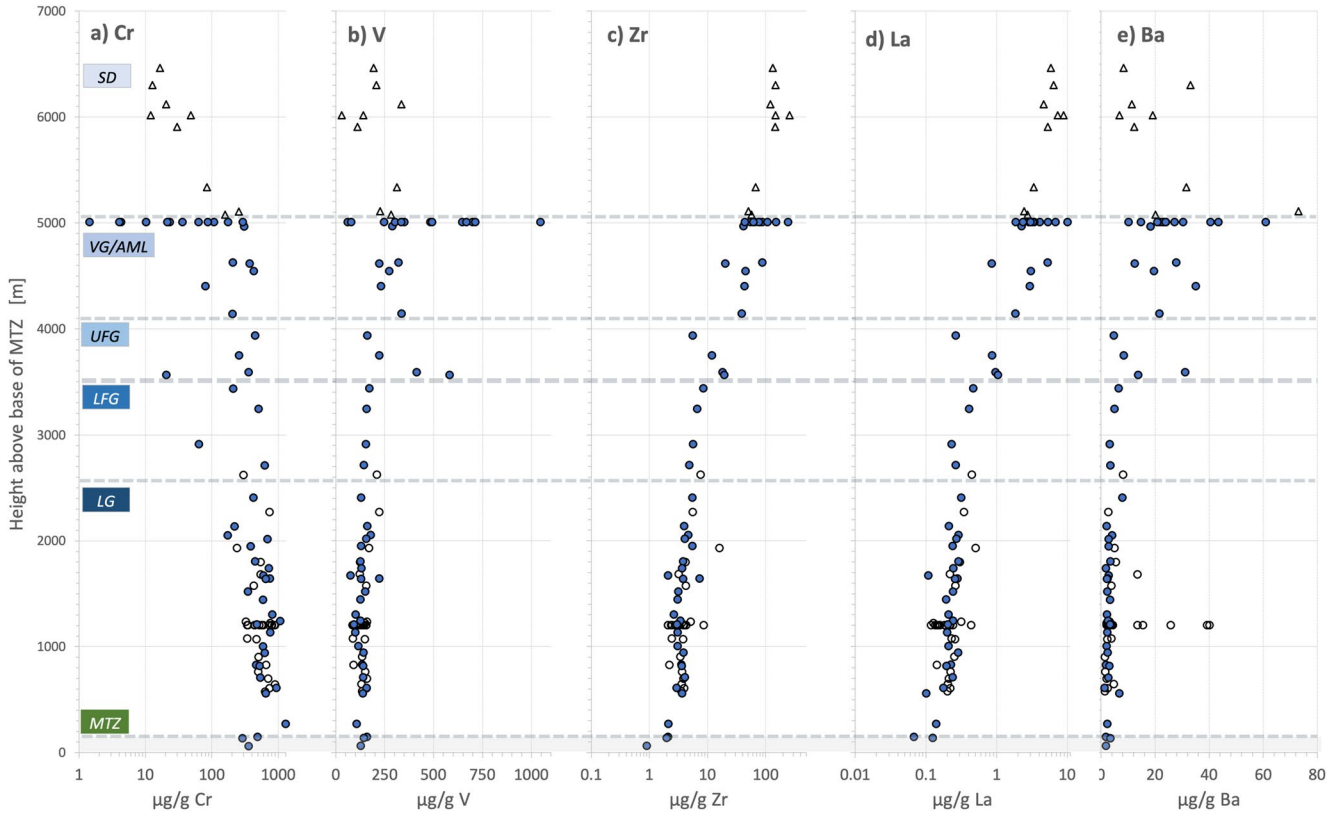

Figure 4. Compositional transects through Wadi Gideah plutonic crust as a function of stratigraphic height over the base of the MTZ: (a) Cr, (b) V, (c) Zr, (d) La, and (e) Ba. Note that plots for Cr, Zr, and La are in log scale. See Figure 3 for legend.

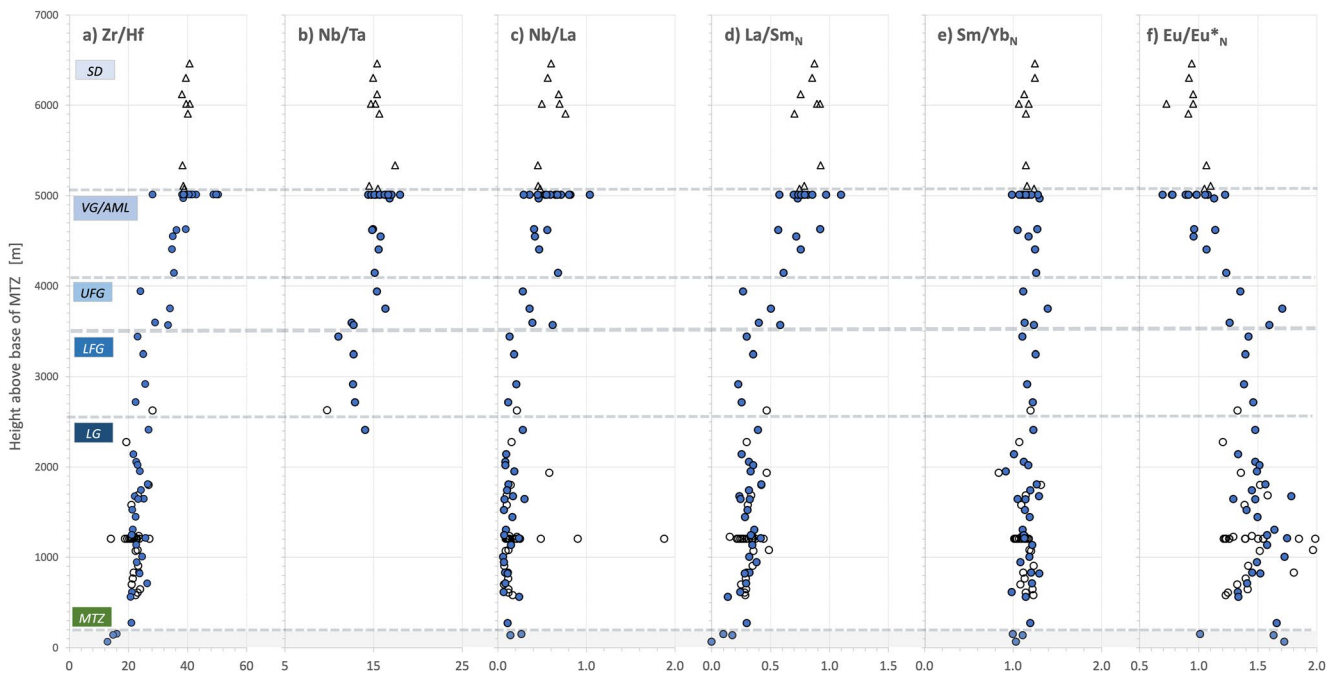

Figure 5. Compositional transects through Wadi Gideah plutonic crust as a function of stratigraphic height over the base of the MTZ: (a) Zr/Hf, (b) Nb/Ta, (c) Nb/La, (d) La/Sm_N, (e) Sm/Yb_N, and (f) Eu/Eu_N*. See Figure 3 for legend.

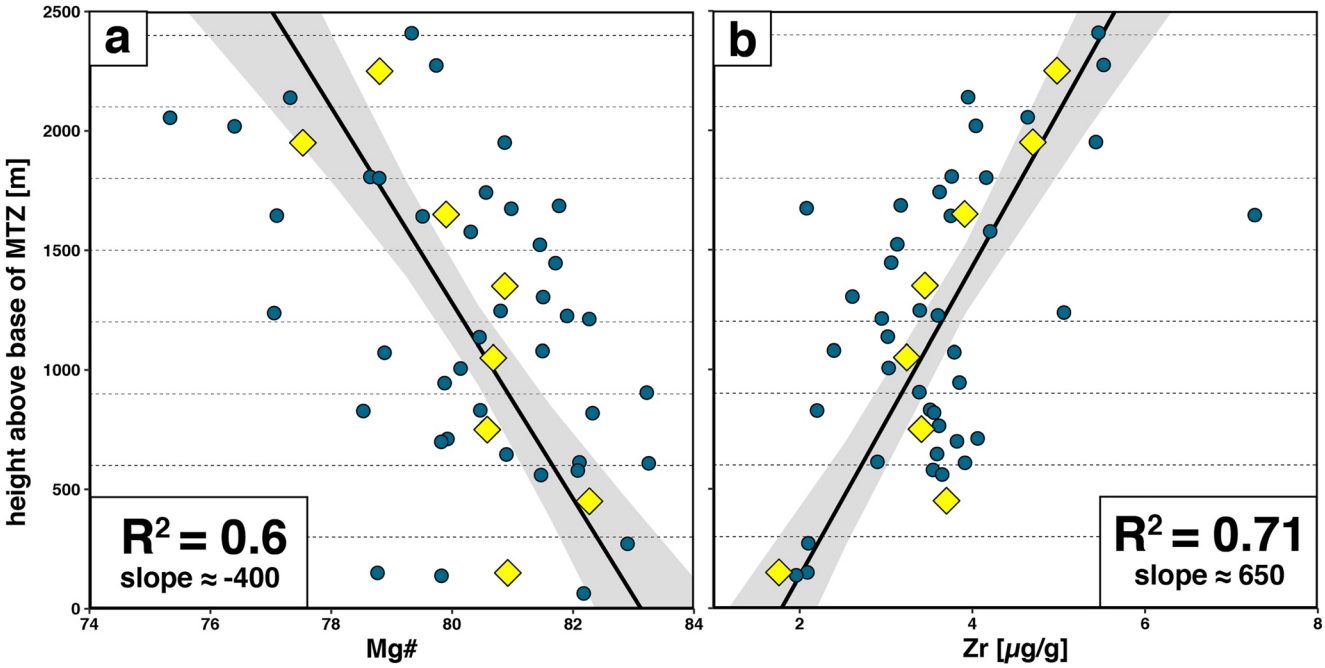

Figure 6. Compositional trends in layered gabbros (LG unit) with increasing distance to the crust/mantle boundary are weak but significant**:** (a) decreasing Mg# shows a significant correlation with increasing height above base of the MTZ over the entire section; (b) Zr shows a similarly significant correlation over the entire transect but is quasi constant below ~1,000 m. *Yellow diamonds* represent averages for 300 m intervals of the transect (stippled horizontal lines). *Slope* is the height interval needed for the change of one unit Mg# and Zr [µg/g], respectively. See text for details.

compared to uppermost LG with Mg# 79 (Supporting Information Data Set S1). The correlation between increasing Mg# in the LG unit and distance from MTZ is weak but significant ($r = 0.774$; $n = 41$; p 0.01; see Figure 6). The slope of this trend indicates a change of Mg# by one unit every ~400 m. This trend of Mg# is much better discernible in mineral chemistry of olivine and clinopyroxene (Koepke et al., 2022: Figure 9). More obvious trends toward differentiated compositions up section are observed in TiO_2 and Na_2O (Figure 2). In contrast, the distribution of SiO_2 and CaO varies by only 1.6 and 5%RSD (1SD), respectively, and no compositional trend is visible (Figure 3). Similar homogeneous distributions are observed for FeO_{tot}, MnO, and Al_2O_3 (Supporting Information Figure S2).

The primitive compositions toward the base of the LG unit are much more visible in high mass fractions of up to 900 µg/g Cr and 200 µg/g Ni (Figure 4) reflecting early precipitates from primitive MORB melts. These values decline rapidly and continue to decrease up section but, exceptions exist at certain depth intervals (see Section 3.1.2). Chromium being a highly compatible element is well correlated with Mg# following trends of fractional crystallization. Such general trends are even more pronounced in distributions of highly incompatible trace elements Zr, La and other LREE, and Th (Figure 4). The correlation of Zr with stratigraphic height over the base of the MTZ is highly significant when calculated over the entire LG + MTZ section, and it takes ~650 m to increase Zr by 1 µg/g (Figure 6). However, Zr remains more or less constant at low mass fractions over the lowermost 1,000 m in the LG unit. The La/Sm ratio increases systematically and synchronous with other incompatible trace elements while the Sm/Yb ratio remains constant over the entire geochemical transect (Figure 5). Similar trends have been observed for light REE and also for P_2O_5 in the Wadi Khafifah transect bulk rock compositions, and Ce in plagioclase and Zr in clinopyroxene exhibit a systematic increase (VanTongeren et al., 2021) similar to what is shown by Müller et al. (2022) for Wadi Gideah. No trend can be observed for V and also Ga, W, Mo, Co, and Zn. The alkali elements Rb, Cs, and K_2O are extremely low in LG and mass fractions are mostly below limits of detection in the lower part of the transect (Table 1).

All LG are characterized by very low average mass fractions of incompatible elements for example, Zr (3.6 µg/g), Hf (0.16 µg/g), Nb (0.024 µg/g), and Th (0.005 µg/g) indicating that reactions with evolved interstitial melts play no significant role in LG composition (Table 1, Supporting Information Figure S2). Detailed petrographic studies confirm that intercumulus phases are virtually absent in LG (Koepke et al., 2022) and compositional zoning from

Table 1
Average Compositions of Lithological Units in the Wadi Gideah Plutonic Crust Transect

	Upper Sheeted Dykes (USD)		Lower Sheeted Dykes (LSD)		Axial Melt Lens (AML)		Varitextured Gabbros (VG)		Upper Foliated Gabbros (UFG)		Lower Foliated Gabbros (LFG)		Layered Gabbors (LG)		Mantle-Crust Transition Zone (MTZ)	
	6		3		16		4		4		4		41		3	
(n)	Md	2SE	Md	2SE	Md	2SE	Md	2SE	Md	2SE	Md	2SE	Md	2SE	Md	2SE
SiO_2	58.96	3.50	52.11	0.66	51.89	3.38	51.08	1.85	47.98	0.20	48.49	0.75	48.15	0.23	49.17	0.25
Al_2O_3	15.21	0.58	16.12	0.40	16.04	0.50	16.18	0.99	18.39	2.31	17.44	0.46	17.88	0.52	17.89	0.49
FeOT	7.98	1.68	9.21	1.33	9.12	1.49	8.40	1.57	7.94	2.16	6.02	0.71	4.82	0.21	4.21	0.83
MnO	0.14	0.04	0.15	0.03	0.13	0.02	0.14	0.02	0.13	0.03	0.12	0.01	0.10	0.004	0.090	0.01
MgO	2.85	1.41	6.96	1.38	5.12	1.10	8.05	0.93	7.92	2.79	9.82	0.77	10.93	0.44	10.70	1.15
CaO	3.97	2.09	9.64	1.08	8.63	1.45	12.46	1.72	14.04	1.76	15.88	1.07	16.88	0.27	16.20	1.52
Na_2O	7.58	0.40	3.52	0.58	4.31	0.79	2.69	0.78	2.29	0.86	1.44	0.46	1.05	0.08	1.59	0.29
K_2O	0.12	0.07	0.22	0.12	0.20	0.04	0.16	0.04	0.058	0.03	0.023	0.00	0.026	0.03	<0.02	
TiO_2	1.70	0.37	1.15	0.19	1.31	0.31	0.94	0.37	1.04	0.63	0.33	0.06	0.25	0.02	0.23	0.07
P_2O_5	0.20	0.03	0.10	0.007	0.12	0.03	<0.08		<0.08		<0.08		<0.08		<0.08	
Total	98.7		99.2		96.9		100.1		99.8		99.6		100.1		100.1	
Mg#	39		57		50		63		64		74		80		82	
Li	1.8	1.2	2.4	0.3	1.3	0.5	1.1	0.4	1.1	0.8	1.1	0.4	0.77	0.1	0.68	0.1
Sc	21	4.4	37	1.0	37	3.6	39	3.6	43	6.3	46	3.4	45	3.0	48	2.1
V	166	84	283	50	416	23	251	52	316	192	155	11	134	10	143	18
Cr	19	11	158	100	22	70	285	157	306	183	357	260	589	71	356	116
Co	11	5.57	35	1.74	32	2.30	39	5.62	39	9.66	41	4.11	36	2.13	41	5.94
Ni	13	5.9	85	27.4	33	13.2	80	19.6	65	61.4	98	48.5	164	16.1	126	22.4
Cu	15	16	16	4	8	51	42	27	58	36	128	55	100	22	60	77
Zn	37	25	36	5	26	7	33	16	49	15	28	6	20	1	16	5
Ga	15	2.2	16	1.5	18	3.9	15	1.1	14	3.2	12	0.9	10	0.3	11	1.2
Rb	0.65	0.46	0.75	0.84	0.86	0.22	0.80	0.55	0.32	0.10	<0.2		0.078	0.04	<0.2	
Sr	100	30	278	71	195	87	152	28	205	42	152	7	140	10	161	55
Y	44	7.7	21	1.8	28	9.5	20	6.4	10	3.5	6.8	1.9	4.7	0.4	4.9	1.4
Zr	147	41	57	10	77	32	41	11	15	6	6.1	2	3.6	0.7	2.0	0.8
Nb	3.6	0.9	1.3	0.2	2.1	0.8	1.3	0.4	0.34	0.2	0.055	0.019	0.024	0.014	0.018	0.001
Mo	2.0	1.5	3.6	5.8	*n.d.*		2.4	2.4	1.3	4.8	0.21	1.1	0.091	0.010	0.087	0.060
Sb	0.031	0.01	0.031	-	*n.d.*		0.024	-	0.024	0.004	0.026	-	0.012	0.002	0.049	-
Cs	0.015	0.007	0.029	0.010	0.013	-	0.015	0.007	0.012	-	0.015	-	0.011	0.003	<0.01	
Ba	12	7.95	32	32.33	24	6.75	20	9.41	11	11.68	4.1	1.50	2.5	0.71	1.7	1.09
Hf	3.7	1.0	1.5	0.26	1.78	0.80	1.2	0.33	0.46	0.19	0.24	0.069	0.16	0.02	0.13	0.04
Ta	0.24	0.06	0.084	0.01	0.124	0.06	0.081	0.03	0.024	0.02	0.005	0.002	0.003	0.002	0.003	0.001
W	0.16	0.08	0.25	0.21	0.05	0.05	0.16	0.09	0.11	0.21	0.068	0.041	0.058	0.013	0.058	0.02
Pb	0.23	0.09	0.11	0.01	0.18	0.60	0.20	0.06	0.16	0.03	0.13	0.009	0.10	0.023	<0.005	
Th	0.39	0.10	0.14	0.07	0.18	0.14	0.11	0.04	0.026	0.01	0.0074	0.003	0.0052	0.003	<0.005	
U	0.13	0.15	0.048	0.00	0.081	0.02	0.036	0.01	0.015	0.007	0.0055	0.007	0.0081	0.002	0.0060	-
La	6.11	1.24	2.72	0.53	3.23	2.1	2.38	1.03	0.90	0.35	0.33	0.11	0.23	0.024	0.10	0.05
Ce	17.0	3.3	7.51	1.2	8.58	5.9	6.66	2.8	2.73	1.0	1.14	0.32	0.74	0.06	0.35	-
Pr	2.87	0.50	1.29	0.16	1.46	0.93	1.16	0.47	0.50	0.17	0.24	0.06	0.15	0.012	0.10	0.01
Nd	14.9	2.3	6.87	0.7	7.83	4.4	6.32	2.4	2.90	1.0	1.55	0.39	1.01	0.07	0.75	0.29

Table 1
Continued

	Upper Sheeted Dykes (USD)		Lower Sheeted Dykes (LSD)		Axial Melt Lens (AML)		Varitextured Gabbros (VG)		Upper Foliated Gabbros (UFG)		Lower Foliated Gabbros (LFG)		Layered Gabbors (LG)		Mantle-Crust Transition Zone (MTZ)	
	6		3		16		4		4		4		41		3	
(n)	Md	2SE	Md	2SE	Md	2SE	Md	2SE	Md	2SE	Md	2SE	Md	2SE	Md	2SE
Sm	4.83	0.69	2.34	0.22	2.60	1.19	2.22	0.78	1.12	0.37	0.70	0.16	0.47	0.032	0.43	0.14
Eu	1.65	0.12	0.93	0.07	0.94	0.32	0.95	0.27	0.72	0.20	0.41	0.09	0.29	0.01	0.19	0.09
Gd	6.30	0.77	3.05	0.31	3.56	1.40	3.01	0.98	1.60	0.52	1.07	0.24	0.73	0.05	0.73	0.21
Tb	1.10	0.19	0.54	0.05	0.63	0.25	0.51	0.17	0.26	0.09	0.18	0.05	0.13	0.011	0.13	0.03
Dy	7.30	1.26	3.52	0.26	4.26	1.65	3.41	1.09	1.73	0.62	1.21	0.34	0.89	0.08	0.88	0.25
Ho	1.63	0.26	0.78	0.07	0.92	0.37	0.73	0.24	0.38	0.14	0.25	0.08	0.18	0.02	0.19	0.05
Er	4.67	0.79	2.23	0.23	2.60	1.12	2.05	0.69	1.06	0.40	0.70	0.22	0.50	0.05	0.53	0.15
Tm	0.70	0.13	0.32	0.03	0.38	0.16	0.31	0.10	0.15	0.06	0.10	0.03	0.070	0.007	0.073	0.02
Yb	4.50	0.85	2.12	0.19	2.55	1.06	1.96	0.67	0.95	0.37	0.64	0.19	0.46	0.04	0.45	0.14
Lu	0.67	0.13	0.31	0.03	0.39	0.16	0.29	0.10	0.14	0.05	0.089	0.03	0.065	0.006	0.063	0.02
Cr/Zr	0.15	0.04	2.8	2.20	1.0	3.54	7.4	7.07	21	34.4	51	54.0	161	32.6	259	147
Zr/Hf	40	0.8	39	0.3	41	0.6	35	0.6	31	4.6	24	1.5	23	0.7	15	1.8
Zr/Y	3.4	0.32	2.7	0.25	3.1	0.31	2.0	0.18	1.2	0.41	0.83	0.07	0.77	0.06	0.35	0.08
Nb/Ta	15	0.3	15	1.7	16	1.3	15	0.4	14	1.9	13	0.9	10	1.1	6.8	2.4
Nb/La	0.65	0.08	0.46	0.02	0.63	0.04	0.51	0.11	0.38	0.15	0.16	0.04	0.12	0.03	0.20	0.10
Y/Ho	28	0.6	28	0.7	30	1.1	27	0.5	26	0.4	26	1.4	26	0.3	26	0.5
La/SmN	0.86	0.07	0.78	0.11	0.82	0.07	0.66	0.09	0.45	0.14	0.28	0.06	0.32	0.02	0.09	0.10
Sm/YbN	1.16	0.06	1.16	0.06	1.12	0.017	1.21	0.10	1.19	0.13	1.19	0.07	1.14	0.03	1.05	0.07
Eu/Eu*N	0.93	0.07	1.06	0.03	0.94	0.12	1.10	0.12	1.48	0.21	1.41	0.04	1.48	0.05	1.46	0.45

Note. Major elements are in [g/100g], trace elements are in [μg/g]; Md: Median; SE: Standard Error; (n): number of analyses; n.d.: not determined.

reaction of cumulus phases with intercumulus melt is only rarely observed in this section. Vanadium has only a very small compatibility in clinopyroxene and can be taken as a tracer for frozen melt trapped as intercumulus phase (Namur et al., 2015). Apart from local excursions in certain short depth intervals, mass fractions of V are very constant over the entire section of LG. This supports the idea that the increasing mass fractions of incompatible elements in LG are not caused by increasing amounts of frozen intercumulus melts but result from in situ fractional crystallization of an evolving melt. This view is confirmed by synchronously evolving mineral core compositions.

The dominant cumulate nature of the LG is reflected in their Zr/Hf ratio of ~21 at the base of the transect. Clinopyroxene is the major cumulus phase in the LG for incorporating Zr and the bulk rock Zr/Hf is mainly controlled by clinopyroxene that has been analyzed by Müller et al. (2022) to Zr/Hf of ~21 in Wadi Gideah LG samples. When using partitioning coefficients of Hart and Dunn (1993) clinopyroxene with Zr/Hf of ~21 would be in equilibrium with a melt having Zr/Hf of ~43. Wadi Gideah samples from the frozen AML and sheeted dikes (Table 1) have Zr/Hf of ~40 comparing well to average N-MORB with Zr/Hf = 41 (Gale et al., 2013). Similarly, Nb/Ta of ~10 in LG corresponds to Nb/Ta of ~15–16 in the AML and sheeted dikes which is in agreement with partitioning coefficients from Bédard (2001) for Nb and Ta in clinopyroxene. Plagioclase being the other major adcumulus phase in LG preferably incorporates Eu over all other REE in its crystal lattice and this is expressed in pronounced positive Eu/Eu^*_N anomalies of all LG in chondrite-normalized plots (Figure 5). The Eu* is calculated from chondrite-normalized REE_N values as the interpolation between Sm_N and Gd_N: $Eu^*_N = (Sm_N + Gd_N)/2$, and the Eu/Eu^*_N anomaly is defined as the ratio of measured Eu_N divided by Eu^*_N.

3.1.2. Sill Injections Reflected in Local and Recurring Deviations From the General Compositional Trends in Layered Gabbros

Superimposed on the general trends toward more differentiated compositions of LG with increasing distance from the MTZ are certain depth intervals in the transect where samples show large compositional variability within short stratigraphic intervals. Especially incompatible elements like LREE, Zr, Hf, Th, and their elemental ratios Zr/Y, Zr/Hf, Nb/La, and La/Yb that are susceptible to fractionation processes reach local maxima at ∼1,200 m, ∼1,950 m, and 2,400–2,600 m above base of the MTZ, but local minima at ∼1,550 m and 2,270 m above base of MTZ (Figures 3–5). Clearly, these observations are biased snapshots with samples taken by chance and at relatively large sampling intervals. However, preliminary results from drill core GT1 taken by the ICDP Oman Drilling Project (Kelemen et al., 2020) show that systematic variability within short dm-sized intervals of many trace elements susceptible to magmatic differentiation processes are typical features of the 400 m long drill core and can be interpreted as resulting from local, recurrent injection of sills into crystal mushes and in situ differentiation and crystallization (Mock, Neave, et al., 2021). Local minima in incompatible element composition may be linked to injection of non-differentiated primitive melts ascending from the crust/mantle boundary.

The injection of sills as the major mechanism during accretion of the lower oceanic crust plays a pivotal role in the Sheeted Sills model of Kelemen et al. (1997) and VanTongeren et al. (2021). Recently, individual melt reservoirs occurring over the entire crustal depth range below the AML have been seismically recorded from the intermediate-spreading Juan de Fuca Ridge (JdF) in a region N 46°45′–47°45′ (Carbotte et al., 2021), interpreted to be embedded within the crystal mush zone underlying the AML. Moreover, at several locations along the EPR and JdF individual magma lenses have been detected that were vertically stacked beneath the spreading ridges. These melt lenses occurred as deep as local MOHO depths and also very shallow, only 100–1,200 m below the AML (e.g., Boddupalli & Canales, 2019; Canales et al., 2009; Carbotte et al., 2021; Marjanovic et al., 2014).

3.1.3. Layered Gabbros Affected by Hydrothermal Fault Zones

Almost all samples of the entire transect are affected to some degree by pervasive alteration that, however, quite often did not notably change their overall composition and can be understood as a kind of hydrothermal overprint. Especially incompatible HFSE and their ratios are stable and not affected by alteration (see "LG-hy" in Supporting Information Data Set S1). These samples are marked with a different signature in our stratigraphic compositional plots in Figures 3–5. The lower part of the layered gabbro section in Wadi Gideah is influenced by more intense hydrothermal activity along well-defined fault zones (HTFZ, high-temperature fault zones) that are vertical to the LG layering and MTZ and occur in more or less regular intervals of 0.5–1 km (e.g., Zihlmann et al., 2018). While samples of such zones are generally characterized by strong greenschist facies overprint showing significant bleaching, some are also affected by a hydrothermal imprint at very high temperature within the magmatic regime, resulting in coarsening of grain size, pegmatoid textures, magmatic hornblende, and accessory oxides and apatites (for details see Koepke et al., 2022). An increased variability of incompatible elements is observed along the 100 m transect through a hydrothermal fracture zone at 1,205 m above base of the MTZ (see Table 1b in Supporting Information Data Set S1) that could be indicative for hydrous melting and local redistribution of elements as a consequence of interaction with hydrothermal fluid. The high crystallization temperatures of hornblende indicate that this hydrothermal activity reached into magmatic temperatures suggesting that this process is closely linked to the formation of the lower plutonic crust (Koepke et al., 2022). Samples from such a hydrothermal fracture zone show a significant shift in their $^{87}Sr/^{86}Sr$ from MORB-type ratios toward seawater signatures (Müller, 2016). Barium being both highly incompatible and a fluid-mobile element is strongly elevated in samples from 1,205 m above mantle-crust boundary (Figure 4), and this is accompanied by a secondary redistribution and enrichment of Nb and Ta (Supporting Information Figure S2) and elevated Nb/La (Figure 5). Copper being highly mobile under hydrothermal conditions reaches its maximum value of 408 µg/g Cu in these samples which compares to 100 µg/g Cu in average LG (cf., Table 1c in Supporting Information Data Set S1; Garbe-Schönberg et al., 2022).

3.2. Lower and Upper Foliated Gabbros and a Compositional Discontinuity at 3,525 m—The Significance of the Foliated-To-Varitextured Gabbro Transition

The last layered gabbro with characteristic modal layering sub-parallel to the MTZ has been sampled from 2,648 m above base of the MTZ and the next sample from 2,671 m is the first sample without any modal layering

but pronounced foliation that is sub-vertical with respect to the orientation of the mantle-crust boundary (Mock, Ildefonse, et al., 2021). The uppermost foliated gabbro (FG) was sampled at 3,939 m above base of the MTZ before foliation vanishes into isotropic gabbros with highly variable textures, the so-called varitextured gabbros. Based on petrography and phase compositions, the LFG are still cumulates with mostly the same mineral assemblage of clinopyroxene, plagioclase, and minor olivine as in the LG unit (Koepke et al., 2022). This is also reflected in their bulk rock chemical composition with a discontinuity at ∼3,525 m above base of the MTZ: samples from the lower foliated gabbros (LFG; 2,648 m up to 3,525 m) have chemical compositions that closely follow the trend established in the LG. In contrast, samples from higher than ∼3,525 m above base of the MTZ in the upper foliated gabbros (UFG; section from 3,525 m up to 4,141 m above base of MTZ, cf., Figure 2) display a significant change toward more evolved compositions. This change in composition is also manifest in a change in texture and crystallographic preferred orientations (Mock, Ildefonse, et al., 2021) being indicative for a change in the magmatic crystallization and depositional regime. The UFG are no longer relatively pure cumulus rocks but rather follow differentiation trends typical for the varitextured gabbros and within the frozen AML and sheeted dikes. This is also visible in the rock texture and in the modal amounts: above this discontinuity, the rocks show significant amounts of interstitial assemblages of late-stage phases Fe-Ti oxides, orthopyroxene, and amphibole (see Figure 4 in Koepke et al., 2022) while they are absent in the (unaltered) lower gabbros.

In the LFG unit, major and trace elements are still closely following the differentiation trends as established in the LG unit and, now, represent the upper end of slightly more differentiated rocks in this evolutionary line of cumulates. Vanadium being a tracer for interstitial phases crystallizing from intercumulus melt is still at constantly low concentrations that are almost the same as in samples from the lowermost LG unit. Consequently, LFG are chemically identical to evolved LG but without exposing the modal layering typical for the LG unit. This implies that the LFG still represent an accretion stage dominated by the accumulation of those minerals of the main stage, cotectic crystallization, and that the in situ freezing of evolved melt from porous flow does not play an essential role.

The situation changes, however, in the UFG unit. This unit starts with a significant and sudden change in elemental compositions at 3,525 m above base of MTZ: especially TiO_2, FeO, and V make a jump to much higher values that correspond to the onset of crystallization of gabbros bearing Fe-Ti oxides as late-stage phases (cf., Figures 3–5). The transition is marked by a significant enrichment of TiO_2 up to 1.72 g/100 g and a TiO_2/Y ratio rising from 0.05 to 0.09 in this unit with the occurrence of Fe-Ti-oxides as interstitial late-stage phase. Similarly, Nb and Nb/La as well as V have a sudden increase while Mg# and also Cr/Zr are much lower than in all other gabbros underneath. This change toward more evolved bulk rock compositions is accompanied by a sudden increase to higher mass fractions of incompatible elements and HFSE: Nb, Ta, LREE, Zr, Th and their ratios Nb/La, La/Yb, Zr/Hf. We see a significant jump from Nb/La 0.14 to 0.62, from Zr/Hf 23.2 to 33.5, from Zr/Y 0.82 to 1.86 when crossing the discontinuity from LFG to UFG. However, the uppermost UFG sample resembles again LFG gabbros in its composition (cf., Figures 3 and 4; Figure 7) thereby giving evidence for a mixing zone between lower and upper gabbros.

All LFG samples and, to a lesser extent, UFG are still characterized by their positive Eu/Eu* anomalies that are interpreted as a chemical signature of abundant cumulus plagioclase. The UFG mark a dramatic change from underlying rocks that were formed almost entirely by in situ crystallization in sill injections from an ascending magma toward overlying varitextured gabbros that crystallized from differentiating magma in the transient and spatially variable AML. This change in crystallization regime can be seen in a plot of Zr/Hf versus Zr (Figure 8): low Zr mass fractions and a Zr/Hf of ∼22 prevailing in the LG and LFG show a significant change within the UFG and varitextured gabbros (VG + AML) toward rapidly increasing Zr mass fractions and Zr/Hf developing toward values of ∼40, typical for average MORB (White & Klein, 2014).

While the CPO results suggest a dominant lineation indicative for vertically transported crystal-laden melts or crystal mushes (Mock et al., 2021) this observation cannot be used for discriminating between down-flow and up-flow directions so that ascending evolved melts from compacting LG cannot be excluded. According to Koepke et al. (2022; Fig. 12), a downward flow of mushes of crystal-laden melts is evident from petrological modeling in order to explain the mineral trends within the UFG and VG unit.

There is another coincidence of observations at the 3,525 m discontinuity: recently estimated equilibrium temperatures for gabbros used in this study via the REE distribution in coexisting plagioclase and clinopyroxene revealed

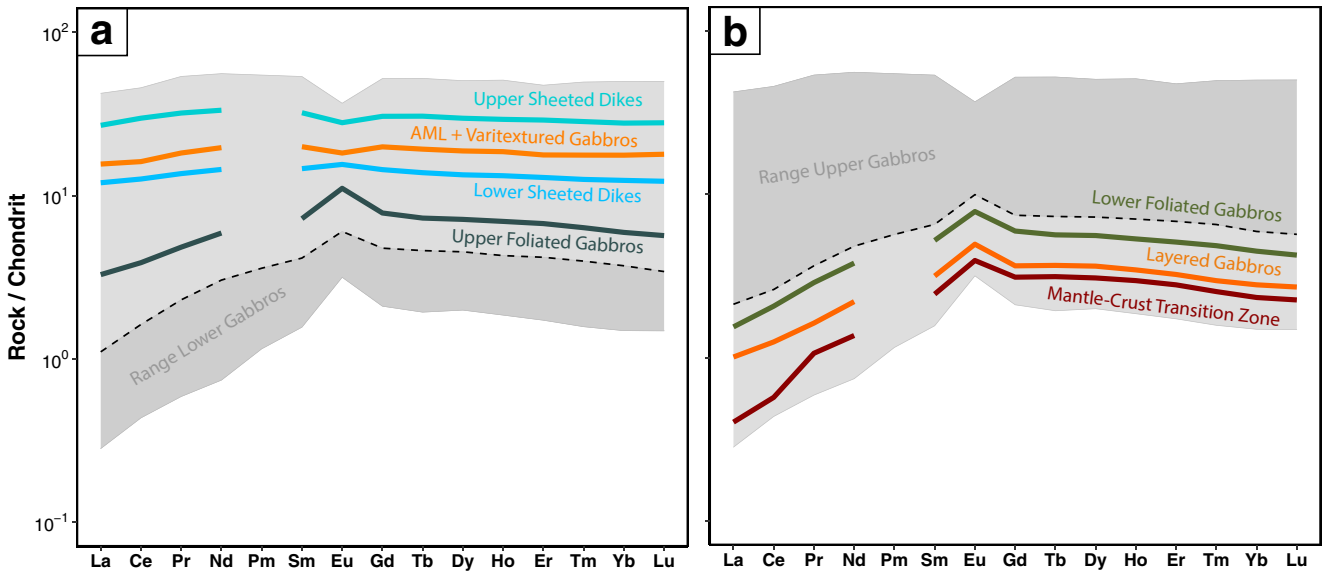

Figure 7. Plots of average REE compositions normalized to chondrite (Sun & McDonough, 1989): (a) upper gabbros above the 3,525 m discontinuity with upper and lower sheeted dikes (USD, LSD), varitextured gabbros and axial melt lens (VG + AML), and upper foliated gabbros (UFG); (b) lower gabbros comprising layered gabbros and gabbros from the mantle-crust transition zone (MTZ). Shaded areas cover REE distributions of all samples in upper and lower gabbros, respectively.

a minimum of crystallization temperatures in this depth range between 3,400 and 3,600 m above base of the MTZ (Müller et al., 2022). The consequences of all these observations for crystallization regimes prevailing in upper and lower gabbros and resulting implications for the mechanisms of accretion of oceanic crust will be discussed in Section 3.4.

We will assign the UFG to the unit of "upper gabbros" in all subsequent estimates for bulk crustal compositions (see Section 3.5). The sample set of VanTongeren et al. (2021) for upper gabbros contains only "transitional gabbros" that are equivalent to our upper foliated gabbros, and no isotropic, varitextured gabbros.

3.3. The Upper Non-Cumulate Gabbros and Sheeted Dikes Root Zone

3.3.1. Varitextured Gabbros and the Frozen AML

Another pronounced change in composition within short stratigraphic distance happens ~600 m above the 3,525 m discontinuity in the pseudo-stratigraphic column at ~4,141 m above base of MTZ at the transition from UFG to VG: while sample OM10-A16 from 3,939 m above base of MTZ has still characteristics of a cumulate and is similar in composition to all underlying LG and LFG rocks by following their evolving compositional trend, the next sample OM10-A15 from 4,144 m is linked to a different trend of fractional crystallization toward the average compositions of the overlying unit of isotropic gabbros or VG hosting a "frozen" AML at 5,009 m (Müller et al., 2017). The pronounced positive Eu/Eu^*_N anomaly being typical for all underlying cumulates rich in plagioclase as in the LG, LFG, and some UFG disappears with sample OM10-A14b from 4,404 m above base of MTZ, and all overlying rocks dominated by "frozen melts" have no, or only small negative or positive, Eu anomalies as a consequence of locally confined differentiation in the AML where mineral segregation does not play a role anymore.

Interestingly, our dedicated comparison of sample preparation techniques (see details in the Supporting Information S1) discovered that complete recovery of Zr by acid digestion failed for rocks containing 40 µg/g Zr or more which can only be explained by the occurrence of zircon crystals that are known to be highly refractory in acid digestion. This mass fraction of 40 µg/g Zr is reached with VG sample OM10-A15 at 4,144 m above base of the MTZ for the first time in the transect and must be interpreted as the first occurrence of crystallized zircons—despite the still very low whole rock mass fraction of Zr. This sample is the first sample when entering the VG from underlying UFG and underlines the sudden change in crystallization regime. The crystallization of zircons

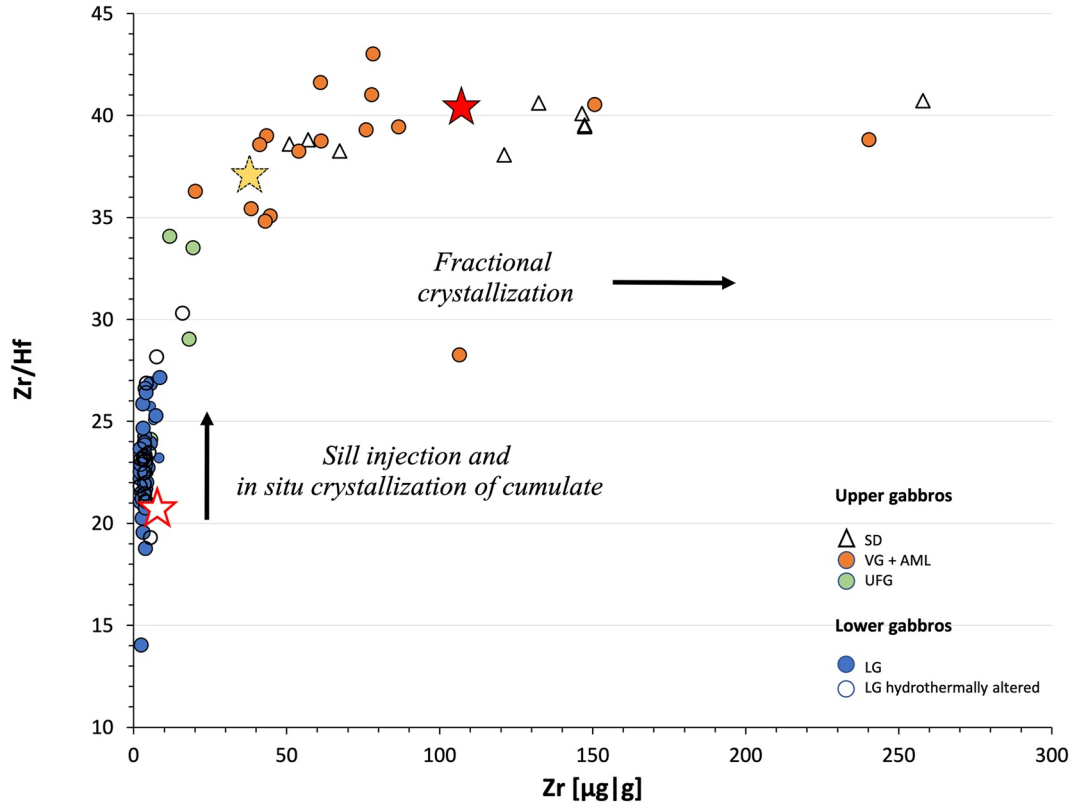

Figure 8. Zr/Hf versus Zr diagram: Upper varitextured gabbros (VG + AML) and sheeted dikes (SD) are highly variable in their Zr as a consequence of fractional crystallization that does not significantly change the Zr/Hf ratio. Values scatter around a Zr/Hf of ~40, typical for mid-ocean ridge basalts (MORB). Layered gabbros (LG) have very low Zr and, with a Zr/Hf ~22, reflect their dominantly cumulate nature. In situ crystallization of ascending melts and differentiating sills causes variability in Zr/Hf but low Zr of LG. Mixing with subsiding crystal mushes above ~3,525 m leads to rapidly increasing Zr in an increasingly melt-dominated transition zone (UFG/VG). *Red star:* MORB (Gale et al., 2013); *Yellow star:* parental magma as calculated from bulk oceanic crust composition (cf., Table 2).

suggests reactions with saturated, highly evolved interstitial melts now playing a major role in upper gabbros, and this is further documented in growth zonations in plagioclase (Koepke et al., 2022; Müller et al., 2022).

The "frozen" AML is characterized by very high lithological variability reaching from domains of rather primitive olivine gabbros and primitive basalts to intrusions of felsic lithologies (quartz diorites, tonalites, trondhjemites) and was studied in detail by Müller et al. (2017). This is reflected in highly variable major and trace element compositions controlled by fractional crystallization processes. Under these conditions in a more closed system the fractionation of incompatible element ratios like Zr/Hf or Nb/La becomes less significant and these ratios are more or less stable at Zr/Hf ~41 and Nb/La ~0.6 (Figure 8, cf., Table 2). It is assumed that the AML was both spatially and temporally transient while building the VG unit and may also vary with respect to the crustal height in a given ridge segment (Carbotte et al., 2013).

3.3.2. Sheeted Dikes and Dike/Gabbro Transition

Sheeted dikes occurring as granoblastic basalt in the lower level (lower sheeted dikes, LSD, for petrography see Koepke et al., 2022) and as altered diabase in higher levels (upper sheeted dikes, USD) do not strictly belong to the plutonic section but represent the MORB-type magma delivered to the ocean floor and must be considered for the calculation of average oceanic crust compositions. They are not well represented in the transect which is due to their sensitivity to weathering and scarcity of outcrops suitable for sampling fresh rocks. While the LSD forming the dike/gabbro transition resemble closely the underlying VG unit in both major and trace element composition, samples from USD are more evolved with higher SiO_2 but also higher in their incompatible elements. Pillow basalts have not been found in Wadi Gideah.

Table 2
Average Compositions of Fast-Spreading Oceanic Crust (Major Elements are in [g/100g], Trace Elements in [µg/g])

	Wadi Gideah				Wadi Khafifah		Jabal Dimh	Hess deep site U1415		Estimated	Modern oceans	
	Upper gabbros 1,280 m	Lower gabbros 3,520 m	Plutonic section 5,010 m	Bulk crust 6,500 m	Bulk plutonic crust§ 5,200 m	Total crustal section§ 7,200 m	Samail ocean crust 7,200 m	Bulk crust ~5,600 m	Plutonic section ~4,600 m	Bulk crust	Lower oceanic crustal sections Average	Lower oceanic crustal sections Median
	(This study)				(van Tongeren et al., 2021)		(Pallister & Gregory, 1983)	(Gillis et al., 2013)		(White & Klein, 2014)	(Coogan, 2014)	
SiO_2	50.8	48.4	49.0	50.5	48.56	49.91	51.1	48.32	47.65	50.1	50.6	51.0
Al_2O_3	16.9	17.8	17.5	17.2	17.58	17.08	16.6	16.71	17.57	15.7	16.7	16.6
FeOT	8.72	5.06	6.14	6.72	6.05	7.30	7.2	7.66	6.47	8.3	7.5	6.1
MnO	0.13	0.10	0.11	0.12	0.11	0.12	0.12	0.14	0.12	0.1	0.14	0.1
MgO	7.09	10.5	9.48	8.59	10.43	8.97	9.2	12.12	13.66	10.3	9.4	9.0
CaO	12.1	16.6	15.2	13.6	15.13	12.84	12.8	11.95	12.35	11.8	12.5	12.6
Na_2O	2.88	1.23	1.72	2.49	1.50	2.39	2.3	1.83	1.56	2.2	2.35	2.4
K_2O	0.12	0.05	0.07	0.10	0.05	0.12	0.12	0.11	0.10	0.11	0.06	0.1
TiO_2	1.14	0.28	0.53	0.69	0.43	0.67	0.60	0.83	0.46	1.1	0.78	0.40
P_2O_5	<0.08	<0.08	<0.08	<0.08		-	0.05	-	-	0.1	0.02	-
Total	99.9	100	99.8	100	99.76	99.36	100.09	100	100	99.8	100	98.3
Mg#	59	79	75	69	75.4	68.7	72	73.8	79.0	72	69	73
Li	1.2	0.88	0.9	1.2						3.5	-	-
Sc	40	48	44	41	*42*					37	37	40
V	321	146	193	204	*157*					299	209	162
Cr	225	544	432	359	*390*					317	308	285
Co	37	40	38	35						31.7	50	41
Ni	61	152	121	106	*144*					134	138	159
Cu	40	110	86	70	*88*					43.7	71	65
Zn	38	23	27	29	*21*					48.5	38	39
Ga	15	11	12	13	*12*					-	14	14
Rb	0.62	0.06	0.22	0.33	*0.26*					1.74	-	-
Sr	185	150	156	168	*149*					103	115	97
Y	18	5.5	9.0	14	*7.6*					18.1	13.9	13
Zr	39	4.4	15	32	*10*					44.5	28.4	28
Nb	1.1	0.033	0.34	0.76	*0.22*					2.77	0.93	1
Mo	1.3	0.13	0.47	1.0						-	-	-
Sb	0.018	0.018	0.017	0.020						-	-	-
Cs	0.013	0.012	0.012	0.015						0.02	-	-
Ba	17	3.03	7.2	11	*7.0*					19.4	-	-
Hf	1.0	0.18	0.43	0.86	*0.35*					1.21	-	-
Ta	0.069	0.003	0.023	0.050						0.18	-	-
W	0.11	0.063	0.08	0.11						-	-	-
Pb	0.18	0.11	0.13	0.13	*1.70*					0.47	-	-
Th	0.093	0.006	0.031	0.078	*0.020*					0.21	-	-
U	0.039	0.008	0.017	0.031	*0.009*					0.07	-	-
La	1.99	0.26	0.76	1.50	*0.52*					2.13	0.86	0.83

Table 2
Continued

	Wadi Gideah				Wadi Khafifah		Jabal Dimh	Hess deep site U1415		Estimated	Modern oceans	
	Upper gabbros 1,280 m	Lower gabbros 3,520 m	Plutonic section 5,010 m	Bulk crust 6,500 m	Bulk plutonic crust§ 5,200 m	Total crustal section§ 7,200 m	Samail ocean crust 7,200 m	Bulk crust ~5,600 m	Plutonic section ~4,600 m	Bulk crust	Lower oceanic crustal sections Average	Median
	(This study)				(van Tongeren et al., 2021)		(Pallister & Gregory, 1983)	(Gillis et al., 2013)		(White & Klein, 2014)	(Coogan, 2014)	
Ce	5.52	0.86	2.21	4.22	*1.58*					5.81	2.75	2.76
Pr	0.96	0.18	0.41	0.74	*0.28*					0.94	0.52	0.53
Nd	5.29	1.18	2.36	4.07	*1.69*					4.90	2.78	2.61
Sm	1.86	0.55	0.92	1.45	*0.66*					1.70	1.10	1.09
Eu	0.85	0.33	0.47	0.64	*0.39*					0.62	0.58	0.58
Gd	2.57	0.85	1.33	2.00	*1.03*					2.25	1.60	1.60
Tb	0.44	0.15	0.23	0.35	*0.19*					0.43	0.31	0.30
Dy	2.93	1.01	1.55	2.32	*1.36*					2.84	2.09	2.06
Ho	0.63	0.21	0.33	0.50	*0.27*					0.63	0.46	0.48
Er	1.78	0.58	0.92	1.42	*0.76*					1.85	1.34	1.32
Tm	0.26	0.082	0.13	0.21	*0.11*					0.28	-	-
Yb	1.70	0.52	0.86	1.35	*0.67*					1.85	1.27	1.23
Lu	0.25	0.074	0.12	0.20	*0.10*					0.28	0.19	0.18
Cr/Zr	6	125	30	11	*39*					7	11	10
Zr/Hf	38	24	34	37	*29*					37	-	-
Zr/Y	2.2	0.80	1.63	2.3	*1.3*					2.5	2.0	2.2
Nb/Ta	15.7	9.9	15.2	15.2						15.4	-	-
Nb/La	0.54	0.13	0.45	0.51	*0.42*					1.30	-	-
Y/Ho	28.1	26.0	27.2	27.2	*28.0*					28.7	30.2	27.1

Note. Major elements are average values in [g/100g], trace elements are median values in [µg/g]; H.a.MTZ: Height above base of mantle-crust transition zone. Lower Gabbros: 0–3,525 m H.a.MTZ, Upper Gabbros: 3,525–5,009 m H.a.MTZ, Plutonic Section: 0–5,009 m H.a.MTZ, Bulk Crust: 0–6,464 m H.a.MTZ. § Trace element data (in italics) are calculated from data reported in Van Tongeren et al., 2021.

3.4. Accretion Processes as Reflected in Bulk Rock Compositions

The general trends observed in the distribution of many elements are interpreted as a result of crystallization from ascending melt batches that evolve with increasing distance from the mantle/crust boundary over the lowermost 3,500 m of the crust, that is, along the layered (LG) and LFG units. This means that either only a relatively small portion of the melt fractionates forming cumulates, or that fractionation is nearly compensated by regular replenishments by more primitive melt, or both. This is also indicated by petrological modeling performed by Koepke et al. (2022). Such replenishments have been proposed by for example, Boudier et al. (1996) or Kelemen et al. (1997). In a more recent study on a drill core obtained from the layered gabbros in Wadi Gideah, Mock, Neave, et al. (2021) presented decameter thick fractionation cycles suggesting that each cycle results from the influx of fresh primitive melt into unconsolidated sill-like structures. The lack of those relatively small-scale trends and some of the lower crustal variability (cf., data from OmanDP drill cores GT1 and GT2, Kelemen et al., 2020) in our profile can be easily explained by the much wider average spacing of ~70 m between adjacent samples in our transect which is not able to resolve finer trends. But, individual samples falling off the general compositional trend in our transect are thought to represent locations with advanced differentiation as in sills (Mock et al., 2020). The ongoing fractionation from the MTZ up to the AML indicates that the melt ascending from the mantle evolves on its way upward, which is consistent with the findings of several previous studies supporting in situ crystallizing sills within the lower oceanic crust (e.g., Boudier et al., 1996; Garrido et al., 2001;

Kelemen & Aharanov, 1998; Kelemen et al., 1997; Korenaga & Kelemen, 1997; VanTongeren et al., 2008). VanTongeren et al. (2021) propose a slightly different model where, after intrusive events, evolved magmas leave the lower gabbros and replenish the upper gabbros thereby contributing to their higher incompatible elements budget.

The average parental magma was in equilibrium with most early-formed cumulus minerals and is similar to primitive mid-ocean ridge basalt (Müller et al., 2022; Pallister & Gregory, 1983). Up to 90 m massive dunites at the mantle-crust transition have been found with drill cores CM1 and CM2, Oman Drilling Project (Kelemen et al., 2020). They can be regarded as early cumulates from a primitive parental MORB melt shifting the composition of the parental melt close to the ol-pl-cpx cotectic in the section of layered gabbros. Observations of heterogenous parental melt intruding the lower crust (Coogan et al., 2002; Gillis et al., 2014) are mainly bound to the early crystallization of orthopyroxene, which is also regarded as indication for mantle/MORB interaction (Coogan et al., 2002). For Wadi Gideah lower crustal gabbros orthopyroxene has a very low (<1%) modal abundance or is fully absent. The continuous and in principal homogeneous evolutional trend of incompatible trace elements (e.g., Zr, Th, Figure 2), systematic decrease of Mg# up-section especially in mineral compositions of olivine and clinopyroxene (Koepke et al., 2022), and constant HREE and Sm/Yb suggest a stable homogeneous magma source likely pooled within the mantle or while crossing the MTZ.

Magma batches passing the MTZ will begin to crystallize the main gabbroic phases olivine, clinopyroxene, and plagioclase rapidly when crossing their respective saturation temperatures (Kelemen & Aharanov, 1998) but only a small fraction of cumulus crystals remains at depth crystallizing in situ while the residual melt mixes with replenishing magma and continues with ascent (Koepke et al., 2022). The density contrast between hot basaltic melt and crystals is highly favorable for a separation of early crystals from ascending melt. The crystallization during liquid flow, sinking and sedimentation of solidifying phases is slow so that crystals can accumulate at depth and practically no liquid is entrapped as intercumulus phase (Namur & Charlier, 2012; Namur et al., 2015). The efficiency of this process is found to decrease with increasing distance to the mantle/crust boundary in a study by Coogan et al. (2002). Reactive porous flow of an interstitial melt as observed at Hess Deep at EPR (Lissenberg et al., 2013) played possibly no significant role which, otherwise, would eventually become visible as interstitial mineral phases trapped from migrating melt, or as extreme zoning. This is not observed in Oman layered gabbros (Koepke et al., 2022; Müller et al., 2022). Major element correlations also hint toward a very limited amount of interstitial reactive melt present within the lower crust, since they would not survive intense melt/rock interactions (Korenaga & Kelemen, 1998). The rising magma is continuously developing into more evolved compositions when rising upwards but the fractionation intensity is low, about 1 Mg# per 400 m stratigraphic height (Müller et al., 2022). This can be explained by repeated replenishment of fresh ascending MORB parental melt with residual, evolved melt in a near steady-state process. Such a process was successfully verified for the lower gabbros by applying petrological modeling based on mineral composition trends (Koepke et al., 2022). Similarly, VanTongeren et al. (2021) propose a model "in which the majority of melt is extracted from lower gabbros." In the Wadi Khafifah transect, however, no such trends are observed in the lower gabbro section (VanTongeren et al., 2021). Besides, this mechanism of low degree crystallization and extraction of the majority of evolving melt can also serve as efficient process for the removal of latent heat from the lower crust (Koepke et al., 2022) which will be transported by the ascending melt rather than by hydrothermal cooling as proposed by Bosch et al. (2004).

The fractionation processes described above require in situ crystallization that basically controls the formation of the lower gabbros below the discontinuity at ~3,525 m above base of the MTZ. In contrast, formation of the upper gabbros is thought to happen in transient melt lenses where fractional crystallization processes in a quasi-closed system can lead to the formation of highly differentiated rocks reaching trondhjemite/plagiogranite compositions (e.g., Müller et al., 2017). Mock, Ildefonse, et al. (2021) suggest a vertical magmatic flow mechanism through the UFG and VG but cannot identify whether such flow occurred up- or downward. Fractionation trends in the upper gabbros, however, suggest that fractionated crystal mushes from the AML(s) mix with ascending melts as documented in the UFG (see also Koepke et al., 2022). In principle, our finding of a two-mechanism accretion model with in situ crystallization in the layered and lower foliated gabbros and a subsiding flow and mixing of evolved crystal mushes from transient AMLs is consistent with the Sheeted Sills model of Kelemen et al. (1997), where a small subsidence mechanism from the AML is also included. However, we infer from our data that about one third of the gabbroic crust accretes by crystallization from the AML, while the two thirds below ~3,525 m

crystallize in situ. The consistency of microstructural, petrological, and geochemical data, and the plausibility of mechanical and chemical processes connecting them, emphasize the robustness of our interpretations.

3.5. Average Composition of the Wadi Gideah Lower Crust and the Composition of Fast-Spreading Oceanic Crust

Bulk-rock compositions provide a way to investigate the processes operating in the lower crust and allow the bulk composition of the lower crust to be estimated which is essential for (a) understanding the processes by which the crust is generated and modified, (c) knowing the average composition of melts crossing the Mantle-crust boundary, and (c) the role of lower oceanic crust in global geochemical cycles (Coogan, 2014; White & Klein, 2014). The average composition of oceanic crust should be directly related to the average parental magma extracted from the mantle.

The first reported mass balance of a complete and clearly cogenetic ophiolite section was SAVE being the Samail AVErage of oceanic crust by Pallister and Gregory (1983). It was calculated as a mass balance from average columnar sections of Jabal Dimh in the Samail ophiolite and has no data from other ophiolites or from the ocean crust (Table 2). Another estimate for bulk lower oceanic plutonic crust and for the total crust section was recently published by VanTongeren et al. (2021) using samples from Wadi Khafifah in the Oman ophiolite, only 10 km west of Wadi Gideah. White and Klein (2014) calculated the average composition of oceanic crust from average MORB compositions as found in the PetDB online data repository but filtered for data quality and used partitioning coefficients from the GERM database for calculating melt composition. Coogan (2014) calculated average and mean compositions for the lower oceanic crust from individual stacked lower oceanic crustal sections as sampled by drill holes and individual grab samples mainly from Pito Deep (Table 2). Gillis et al. (2013) presented an average for the bulk fast-spreading oceanic crust from stacked drill cores recovered by IODP at the Hess Deep Rift at EPR, in combination with basalts sampled by ship expeditions in the same area. Our data set for major and trace elements in lower oceanic and bulk oceanic crust as presented in Table 2 was calculated from weighted means (major elements) and medians (trace elements) of individual lithological units in the Wadi Gideah transect. The weighting factors were calculated from the relative proportions of thicknesses of the crustal units as shown in Figure 2. Geochemical signatures of upper crustal sheeted dikes and pillow basalts (Müller, 2016) indicate a typical MOR setting with a component from an early stadium of subduction zone initiation (MacLeod et al., 2013).

The fractionation of elements between the upper basaltic and lower plutonic crust is well known and clearly visible in our data (Table 2). The lower crust is highly depleted in incompatible elements as a consequence of fractionation and missing intercumulus phases originating from interstitial melts during reactive porous flow. Bulk rock partitioning coefficients for, for example, HFSE calculated as elemental ratios of lower gabbros divided by upper crustal varitextured gabbros and sheeted dikes come close to values experimentally determined for the minerals involved (i.e., mainly clinopyroxene). This can be interpreted as a very efficient separation of melt from cumulus crystals crystallizing in situ in layered gabbros in the lower crust, and confirms our conclusion that interstitial phases from frozen trapped melts and other indications for reactive porous flow do not play an important role.

Our calculated average compositions for the entire 6,500 m of bulk oceanic crust comprising sheeted dikes and all varieties of gabbros down to the MTZ mimic the old SAVE data from Pallister and Gregory (1983) and are very similar to their values for major elements and Mg#, and many of our median trace element compositions are similar to data published by Coogan (2014). Only REE are significantly higher in our data. When compared to values published by White and Klein (2014) it becomes evident that their bulk composition is slightly more primitive with Mg# 72 with elevated Ni, V and lower CaO, Sr which might be related to the fact that ultramafic cumulates are basically missing in our Wadi Gideah profile. The HFSE elements Zr, Hf, Th, Nb, Ta, and Ba, however, are significantly higher and REE are highest in their data when compared to all other data. A detailed comparison of our data with new data from VanTongeren et al. (2021) shows striking similarities of both major and trace element mass fractions in the plutonic sections, and also the discontinuity between lower and upper gabbros is found at a similar depth at ~3,700 m above base of MTZ. This finding is significant and demonstrates the robustness and consistency of both data sets. It also hints toward the continuity of the accretion processes in both space and time. The two Wadis are ~10 km apart from each other, and if this distance were along strike it would correspond to a time interval of ~100,000–200,000 years assuming a half-spreading rate of 5–10 cm/year.

4. Conclusions

We sampled a transect through 6.5 km of fossil oceanic crust of the Samail ophiolite (Sultanate of Oman, Wadi Gideah). Here we report a full set of whole rock major and trace element data displaying systematic and contrasting compositional trends that are correlated with stratigraphic depth in the plutonic suite. All samples have been analyzed at least twice using both solution-based and direct solids analytical techniques.

The striking feature of our compositional transect through the entire plutonic section of fossil oceanic crust in the Samail ophiolite is the steady development toward more evolved rock compositions with increasing distance from MTZ into the upper gabbros as a consequence of fractionation of a basaltic parental magma. While these trends are barely discernible but statistically significant for some elements, and easily recognizable for incompatible elements and their ratios in the lower gabbros, especially incompatible elements show a dramatic increase in the upper gabbros. Superimposed on these general trends in the lower, dominantly cumulate gabbros are higher compositional variabilities at discrete depth intervals that are thought to reflect intrusion and in situ fractionation of sills. In contrast, upper, non-cumulate gabbros forming the isotropic varitextured gabbros in the uppermost gabbros, and special lithologies within a "frozen" melt lens horizon show much higher compositional variability and differentiation trends from fractionated crystallization in a quasi-closed system. Microstructural evidence (Mock, Ildefonse, et al., 2021) combined with fractionation trends in mineral composition (major elements: Koepke et al., 2022; trace elements: Müller et al., 2022) and the bulk rock geochemical data of this study suggest that crystal mushes originating from the AML subside and mix in the upper foliated gabbros with ascending melts. A significant change between the two crystallization regimes is expressed in a discontinuity in geochemical composition as well as in microstructures and localized at ∼3,525 m height above base of the MTZ, which is in the middle of the lithological unit of foliated gabbros with near vertical lineation. This is also the zone where Müller et al. (2022) found a minimum in crystallization temperatures during the magmatic accretion of the Oman paleocrust. Main conclusions of our findings are:

1. All lower gabbros below ∼3,525 m above the base of MTZ have very low mass fractions of incompatible elements, for example, Zr, Hf, Nb, Ta, Th, LREE that develop with distance from MTZ to more differentiated compositions while Mg# number, especially in the minerals clinopyroxene and olivine (Koepke et al., 2022), slightly decreases. Elemental ratios, for example, Zr/Hf, Zr/Y, Nb/La, etc. develop synchronously. It is suggested that such behavior of trace element composition, HFSE elemental ratios, and also of Mg# number is a consequence of efficient separation of in situ crystallizing cumulus phases from a constantly evolving, ascending parental melt. There is no intercumulus phase in layered gabbros that could have formed from crystallizing interstitial melt, and this becomes evident from the very low mass fractions of incompatible elements, from low V as a proxy for interstitial melt, and from petrographic studies (Koepke et al., 2022). Superimposed on the general trend are higher compositional variabilities over short stratigraphic intervals that are suggested to represent advanced in situ crystallization/fractionation of sill injections.
2. All upper gabbros above ∼3,525 m above base of MTZ with isotropic and non-lineated microstructures, including sheeted dikes, are controlled by fractional crystallization processes in a magma chamber where strong fractionation trends are developing but with minor or no fractionation of HFSE elemental ratios.
3. The transition between these two crystallization regimes is a sharp discontinuity at ∼3,525 m height above base of MTZ and lies within mostly vertically lineated foliated gabbros.

Our finding of a two-mechanisms accretion model sensu Koepke et al. (2022) with in situ crystallization in the layered and lower foliated gabbros, and a subsidence transport of evolved crystal mush from the AML in the upper foliated and isotropic gabbros is a hybrid model combining ideas of the Gabbro Glacier model (e.g., Henstock et al., 1993) for the upper part and ideas from the Sheeted Sills model (e.g., Kelemen et al., 1997; VanTongeren et al., 2021) for the lower part. However, the Sheeted Sills model of Kelemen et al. (1997) includes a small subsidence mechanism from the AML. We infer from our data that about one third of the plutonic crust accretes in the upper gabbros as subsiding mush from the AML, while the two thirds below crystallize in situ in lower gabbros.

New average compositions of (paleo-) oceanic crust are reported for major and 38 trace elements that basically agree with older data from modeling and from stacked drill holes for the composition of oceanic crust. Distribution especially of incompatible elements illustrates the strong fractionation between lower and upper gabbros.

The striking similarity of observations for sections in Wadi Gideah and Wadi Khafifah (VanTongeren et al., 2021) is significant and suggests robustness and continuity of accretion processes in both space and time.

Data Availability Statement

Data produced for this work and discussed within this study are available on the FAIR-aligned Pangaea repository: https://doi.org/10.1594/PANGAEA.942970.

Acknowledgments
The study benefitted greatly from critical and constructive reviews by John Lassiter and one anonymous reviewer who is kindly acknowledged. The authors highly appreciate the support of the Oman Public Authority for Mining for permission of conducting fieldwork in Oman. Special thanks go to Dr. Ali Al Rajhi, Dr. Mohamed Al Batashi, and Dr. Mohamed Al Araimi. We kindly thank Prof. Dr. Sobhi Nasir, Geology Department of Sultan Quaboos University for generous assistance during planning and conducting fieldwork, and shipping samples. Help from Ulrike Westernströer with ICP-MS and LA-ICP-MS, Karen Bremer with ICP-OES, and Leewe Schönberg with LA-ICPMS is highly appreciated. Jasper Berndt-Gerdes (U Münster) provided access to his strip heater facility and Stefan Jung (U Hamburg) contributed to XRF data. This work was funded by the Deutsche Forschungsgemeinschaft (DFG, German Research Foundation) by a grant given to DGS and JK, Project No.: 214851514, GA 1960/11-2, KO 1723/21-2. Open Access funding enabled and organized by Projekt DEAL.

References

Alabaster, T., Pearce, J. A., & Malpas, J. (1982). The volcanic stratigraphy and petrogenesis of the Oman Ophiolite Complex. *Contributions to Mineralogy and Petrology*, *81*, 168–183. https://doi.org/10.1007/bf00371294

Alt, J. C., Laverne, C., Vanko, D., Tartarotti, P., Teagle, D. A. H., Bach, W., et al. (1996). Hydrothermal alteration of a section of upper oceanic crust in the eastern equatorial Pacific: A synthesis of results from DSDP/ODP Legs 69, 70, 83, 111, 137, 140, 148 at site 504B. *Proceedings of the Ocean Drilling Program, Scientific Results*, *148*, 417–434.

Anonymous. (1972). Penrose field conference: Ophiolites. *Geotimes*, *17*, 24–25.

Bédard, J. H. (2001). Parental magmas of the Nain Plutonic Suite anorthosites and mafic cumulates: A trace element modelling approach. *Contributions to Mineralogy and Petrology*, *141*(6), 747–771.

Bédard, J. H., Sparks, R. S. J., Renner, R., Hunter, R., & Cheadle, M. (1988). A re-evaluation of the origin and nature of layered peridotite, troctolite and gabbro in the Eastern Layered Series of the Rhum ultrabasic complex, Inner Hebrides. *Geological Society, London, Special Publications*, *39*(1), 391.

Boddupalli, B., & Canales, J. P. (2019). Distribution of crustal melt bodies at the hot spot-influenced section of the Galápagos Spreading Centre from seismic reflection images. *Geophysical Research Letters*, *46*(9), 4664–4673. https://doi.org/10.1029/2019gl082201

Bosch, D., Jamais, M., Boudier, F., Nicolas, A., Dautria, J.-M., & Agrinier, P. (2004). Deep and high-temperature hydrothermal circulation in the Oman ophiolite – Petrological and isotopic evidence. *Journal of Petrology*, *45*, 1181–1208. https://doi.org/10.1093/petrology/egh010

Botcharnikov, R. E., Holtz, F., Mungall, J. E., Beermann, O., Linnen, R. L., & Garbe-Schönberg, D. (2013). Behavior of gold in a magma at sulfide-sulfate transition: Revisited. *American Mineralogist*, *98*(8–9), 1459–1464. https://doi.org/10.2138/am.2013.4502

Boudier, F., Ceuleneer, G., & Nicolas, A. (1988). Shear zones, thrusts and related magmatism in the Oman ophiolite: Initiation of thrusting on an oceanic ridge. *Tectonophysics*, *151*(1–4), 275–296. https://doi.org/10.1016/0040-1951(88)90249-1

Boudier, F., Nicolas, A., & Ildefonse, B. (1996). Magma chambers in the Oman ophiolite: Fed from the top and the bottom. *Earth and Planetary Science Letters*, *144*(1–2), 239–250. https://doi.org/10.1016/0012-821x(96)00167-7

Canales, J. P., Detrick, R. S., Toomey, D. R., & Wilcock, W. S. D. (2003). Segment-scale variations in the crustal structure of 150-300 kyr old fast spreading oceanic crust (East Pacific Rise, 8 degrees 15 ' N-10 degrees 5 ' N) from wide-angle seismic refraction profiles. *Geophysical Journal International*, *152*, 766–794.

Canales, J. P., Nedimović, M. R., Kent, G. M., Carbotte, S. M., & Detrick, R. S. (2009). Seismic reflection images of a near-axis melt sill within the lower crust at the Juan de Fuca ridge. *Nature*, *460*(7251), 89–93. https://doi.org/10.1038/nature08095

Cann, J. R. (1974). Model for oceanic crustal structure developed. *Geophysical Journal of the Royal Astronomical Society*, *39*(1), 169–187. https://doi.org/10.1111/j.1365-246X.1974.tb05446.x

Carbotte, S. M., Marjanović, M., Arnulf, A. F., Nedimović, M. R., Canales, J. P., & Arnoux, G. M. (2021). Stacked magma lenses beneath mid-ocean ridges: Insights from new seismic observations and synthesis with prior geophysical and geologic findings. *Journal of Geophysical Research: Solid Earth*, *126*(4), e2020JB021434. https://doi.org/10.1029/2020jb021434

Carbotte, S. M., Marjanović, M., Carton, H., Mutter, J. C., Canales, J. P., Nedimović, M. R., & Perfit, M. R. (2013). Fine-scale segmentation of the crustal magma reservoir beneath the East Pacific Rise. *Nature Geoscience*, *6*(10), 866–870. https://doi.org/10.1038/ngeo1933

Chen, J. H., & Pallister, J. S. (1981). Lead isotopic studies of the Samail ophiolite, Oman. *Journal of Geophysical Research*, *86*(NB4), 2699–2708. https://doi.org/10.1029/jb086ib04p02699

Coleman, R. G. (1981). Tectonic setting for ophiolite obduction in Oman. *Journal of Geophysical Research*, *86*(NB4), 2497–2508. https://doi.org/10.1029/jb086ib04p02497

Coogan, L. A. (2014). 4.14 – The lower oceanic crust. In H. D. Holland, & K. K. Turekian (Eds.), *Treatise on geochemistry* (2nd ed., pp. 497–541). Oxford: Elsevier. https://doi.org/10.1016/b978-0-08-095975-7.00316-8

Coogan, L. A., Jenkin, G. R. T., & Wilson, R. N. (2002). Constraining the cooling rate of the lower oceanic crust: A new approach applied to the Oman ophiolite. *Earth and Planetary Science Letters*, *199*(1–2), 127–146. https://doi.org/10.1016/s0012-821x(02)00554-x

Detrick, R. S., Buhl, P., Vera, E., Mutter, J., Orcutt, J., Madsen, J., & Brocher, T. (1987). Multichannel seismic imaging of a crustal magma chamber along the East Pacific Rise. *Nature*, *326*, 35–41. https://doi.org/10.1038/326035a0

Dick, H. J. B., Natland, J. H., & Ildefonse, B. (2006). Deep drilling in the oceanic crust and mantle. *Oceanography*, *19*, 74–82. https://doi.org/10.5670/oceanog.2006.06

Fricker, M. B., Kutscher, D., Aeschlimann, B., Frommer, J., Dietiker, R., Bettmer, J., & Günther, D. (2011). High spatial resolution trace element analysis by LA-ICP-MS using a novel ablation cell for multiple or large samples. *International Journal of Mass Spectrometry*, *307*(1–3), 39–45. https://doi.org/10.1016/j.ijms.2011.01.008

Gale, A., Dalton, C. A., Langmuir, C. H., Su, Y., & Schiling, J. (2013). The mean composition of ocean ridge basalts. *Geochemistry, Geophysics, Geosystems*, *14*(3). https://doi.org/10.1029/2012GC004334

Garbe-Schönberg, D. (1993). Simultaneous determination of 37 trace elements in 28 international rock standards by ICP-MS. *Geostandards Newsletter*, *17*(1), 81–97. https://doi.org/10.1111/j.1751-908X.1993.tb00122.x

Garbe-Schönberg, D., Koepke, J., Müller, S., Mock, D., & Müller, T. (2022). *Wadi Gideah, Oman, reference section: Whole rock geochemistry*. PANGAEA. https://doi.org/10.1594/PANGAEA.942970

Garbe-Schönberg, D., & Müller, S. (2014). Nano-particulate pressed powder tablets for LA-ICP-MS. *Journal of Analytical Atomic Spectrometry*, *29*(6), 990–1000. https://doi.org/10.1039/c4ja00007b

Garrido, C. J., Kelemen, P. B., & Hirth, G. (2001). Variation of cooling rate with depth in lower crust formed at an oceanic spreading ridge: Plagioclase crystal size distributions in gabbros from the Oman ophiolite. *Geochemistry, Geophysics, Geosystems*, *2*, 2000GC000136. https://doi.org/10.1029/2000gc000136

Gillis, K., Snow, J., Klaus, A., Guerin, G., Abe, N., Akizawa, N., et al. (2014). Expedition 345 summary. Paper presented at the Proceedings of the integrated ocean drilling Program. https://doi.org/10.2204/iodp.proc.345.101.2014

Gillis, K. M., Snow, J. E., Klaus, A., Abe, N., Adriao, A. B., Akizawa, N., et al. (2013). Primitive layered gabbros from fast-spreading lower oceanic crust. *Nature*, *505*(7482), 204–207. https://doi.org/10.1038/nature12778

Goodenough, K. M., Thomas, R. J., Styles, M. T., Schofield, D. I., & MacLeod, C. J. (2014). Records of ocean growth and destruction in the Oman-UAE ophiolite Elements, *10*(2), 109–114. https://doi.org/10.2113/gselements.10.2.109

Gregory, R. T., & Taylor, H. P. (1981). An oxygen isotope profile in a section of Cretaceous oceanic crust, Semail ophiolite, Oman: Evidence for d18 O buffering of the ocean by deep (> 5 km) seawater hydrothermal circulation at Mid-Ocean Ridges. *Journal of Geophysical Research*, *86*, 2737–2755. https://doi.org/10.1029/jb086ib04p02737

Hart, S. R., & Dunn, T. (1993). Experimental cpx/melt partitioning of 24 trace elements. *Contributions to Mineralogy and Petrology*, 113, 1–8. https://doi.org/10.1007/bf00320827

Henstock, T. J., Woods, A. W., & White, R. S. (1993). The accretion of oceanic crust by episodic sill intrusion. *Journal of Geophysical Research*, *98*(B3), 4143–4161. https://doi.org/10.1029/92jb02661

Hopson, C. A., Coleman, R. G., Gregory, R. T., Pallister, J. S., & Bailey, E. H. (1981). Geologic section through the Samail ophiolite and associated rocks along a Muscat-Ibra transect, southern Oman mountains. *Journal of Geophysical Research*, *86*(NB4), 2527–2544. https://doi.org/10.1029/jb086ib04p02527

Kelemen, P., Matter, J., Teagle, D., Coggon, J., & the Oman Drilling Project Science Team. (2020). *Proceedings of the Oman drilling project*. International Ocean Discovery Program. https://doi.org/10.14379/OmanDP.proc.2020

Kelemen, P. B., & Aharanov, E. (1998). Periodic formation of magma fractures and generation of layered gabbros in the lower crust beneath oceanic spreading ridges. *Geophysical Monograph – American Geophysical Union*, *106*, 267–290.

Kelemen, P. B., Koga, K., & Shimizu, N. (1997). Geochemistry of gabbro sills in the crust-mantle transition zone of the Oman ophiolite: Implications for the origin of the oceanic lower crust. *Earth and Planetary Science Letters*, *146*(3–4), 475–488. https://doi.org/10.1016/s0012-821x(96)00235-x

Koepke, J., Feig, S. T., Berndt, J., & Neave, D. A. (2021). Wet magmatic processes during the accretion of the deep crust of the Oman Ophiolite paleoridge: Phase diagrams and petrological records. *Tectonophysics*, *817*. https://doi.org/10.1016/j.tecto.2021.229051

Koepke, J., Garbe-Schönberg, D., Müller, T., Mock, D., Müller, S., & Nasir, S. (2022). A reference section through fast-spread lower oceanic crust, Wadi Gideah, Samail ophiolite (Sultanate of Oman): Petrography and petrology. *Journal of Geophysical Research: Solid Earth*, *127*(1). https://doi.org/10.1029/2021JB022735

Koepke, J., Schoenborn, S., Oelze, M., Wittmann, H., Feig, S., Hellebrand, E., et al. (2009). Petrogenesis of crustal wehrlites in the Oman ophiolite: Experiments and natural rocks. *Geochemistry, Geophysics, Geosystems*, *10*. https://doi.org/10.1029/2009GC002488

Korenaga, J., & Kelemen, P. B. (1997). Origin of gabbro sills in the Moho transition zone of the Oman ophiolite: Implications for magma transport in the oceanic lower crust. *Journal of Geophysical Research*, *102*(B12), 27729–27749. https://doi.org/10.1029/97jb02604

Korenaga, J., & Kelemen, P. B. (1998). Melt migration through the oceanic lower crust: A constraint from melt percolation modeling with finite solid diffusion. *Earth and Planetary Science Letters*, *156*, 1–11. https://doi.org/10.1016/s0012-821x(98)00004-1

Lissenberg, C. J., & Dick, H. J. B. (2008). Melt-rock reaction in the lower oceanic crust and its implications for the genesis of mid-ocean ridge basalt. *Earth and Planetary Science Letters*, *271*(1–4), 311–325. Retrieved from <Go to ISI>://000257835600031. https://doi.org/10.1016/j.epsl.2008.04.023

Lissenberg, C. J., MacLeod, C. J., Howard, K. A., & Godard, M. (2013). Pervasive reactive melt migration through fast-spreading lower oceanic crust (Hess Deep, equatorial Pacific Ocean). *Earth and Planetary Science Letters*, *361*, 436–447. https://doi.org/10.1016/j.epsl.2012.11.012

Maclennan, J., Hulme, T., & Singh, S. C. (2004). Thermal models of oceanic crustal accretion: Linking geophysical, geological and petrological observations. *Geochemistry, Geophysics, Geosystems*, *5*, 2003GC000605. https://doi.org/10.1029/2003gc000605

MacLeod, C. J., Lissenberg, C. J., & Bibby, L. E. (2013). "Moist MORB" axial magmatism in the Oman ophiolite: The evidence against a mid-ocean ridge origin. *Geology*, *41*(4), 459–462. https://doi.org/10.1130/g33904.1

MacLeod, C. J., & Yaouancq, G. (2000). A fossil melt lens in the Oman ophiolite: Implications for magma chamber processes at fast spreading ridges. *Earth and Planetary Sciences Letters*, *176*, 357–373. https://doi.org/10.1016/s0012-821x(00)00020-0

Marjanovic, M., Carbotte, S. M., Carton, H., Nedimovic, M. R., Mutter, J. C., & Canales, J. P. (2014). A multi-sill magma plumbing system beneath the axis of the East Pacific Rise. *Nature Geoscience*, *7*(11), 825–829. https://doi.org/10.1038/ngeo2272

McCulloch, M. T., Gregory, R. T., Wasserburg, G. J., & Taylor, H. P. (1981). Sm-Nd, Rb-Sr, and $^{18}O/^{16}O$ systematics in an oceanic crustal section: Evidence from the Samail Ophiolite. *Journal of Geophysical Research*, *86*(B4), 2721–2735. https://doi.org/10.1029/jb086ib04p02721

Mock, D., Ildefonse, B., Müller, T., & Koepke, J. (2021). A reference section through fast-spread lower oceanic crust, Wadi Gideah, Samail ophiolite (Sultanate of Oman): Insights from crystallographic preferred orientations. *Journal of Geophysical Research: Solid Earth*, *126*, e2021JB021864. https://doi.org/10.1029/2021JB021864

Mock, D., Neave, A. D., Müller, S., Garbe-Schönberg, D., Ildefonse, B., & Koepke, J. (2021). Accretion of fast-spread lower oceanic crust: Drill core GT1 from the ICDP Oman Drilling Project. Paper presented at the EGU General Assembly Conference Abstracts.

Mock, D., Neave, D., Müller, S., Garbe-Schönberg, D., Namur, O., Ildefonse, B., & Koepke, J. (2020). Formation of igneous layering in the lower oceanic crust from the Samail Ophiolite, Sultanate of Oman. *Journal of Geophysical Research: Solid Earth*, e2020JB019573. https://doi.org/10.1029/2021JB019573

Müller, S., Garbe-Schönberg, D., Koepke, J., & Hoernle, K. (2022). A reference section through fast-spread lower oceanic crust, Wadi Gideah, Samail Ophiolite (Sultanate of Oman): Trace element systematics and crystallization temperatures - Implications for hybrid crustal accretion. *Journal of Geophysical Research: Solid Earth*, *127*, e2021JB022699. https://doi.org/10.1029/2021JB022699

Müller, T. (2016). A petrological and geochemical cross section of lower crust at the Wadi Gideah (Samail ophiolite): Implications for the crustal accretion at fast-spreading mid-ocean ridges. (PhD Thesis). University of Hannover.

Müller, T., Koepke, J., Garbe-Schönberg, C. D., Dietrich, M., Bauer, U., & Wolff, P. E. (2017). Anatomy of a frozen axial melt lens from a fast-spreading paleo-ridge (Wadi Gideah, Oman ophiolite). *Lithos*, *272–273*, 31–45. https://doi.org/10.1016/j.lithos.2016.11.022

Namur, O., Abily, B., Boudreau, A. E., Blanchette, F., Bush, J. W. M., Ceuleneer, G., et al. (2015). Igneous layering in basaltic magma chambers. In B. Charlier (Ed.), *Layered intrusions*. Springer Geology. https://doi.org/10.1007/978-94-017-9652-1

Namur, O., & Charlier, B. (2012). Efficiency of compaction and compositional convection during mafic crystal mush solidification: The Sept Iles layered intrusion, Canada. *Contributions to Mineralogy and Petrology*, *163*, 1049–1068. https://doi.org/10.1007/s00410-011-0715-3

Natland, J. H., & Dick, H. J. B. (2009). Paired melt lenses at the East Pacific Rise and the pattern of melt flow through the gabbroic layer at a fast-spreading ridge. *Lithos*, *112*(1–2), 73–86. https://doi.org/10.1016/j.lithos.2009.06.017

Nicolas, A., Boudier, F., Ildefonse, B., & Ball, E. (2000). Accretion of Oman and United Arab Emirates ophiolite – Discussion of a new structural map. *Marine Geophysical Researches*, *21*(3–4), 147–179. https://doi.org/10.1023/a:1026769727917

Nicolas, A., & Poliakov, A. (2001). Melt migration and mechanical state in the lower crust of oceanic ridges. *Terra Nova*, *13*(1), 64–69. https://doi.org/10.1046/j.1365-3121.2001.00319.x

Pallister, J. S., & Gregory, R. T. (1983). Composition of the Samail ocean crust. *Geology*, *11*(11), 638–642. https://doi.org/10.1130/0091-7613(1983)11<638:cotsoc>2.0.co;2

Pallister, J. S., & Hopson, C. A. (1981). Samail Ophiolite plutonic suite: Field relations, phase variation, cryptic variation and layering, and a model of a spreading ridge magma chamber. *Journal of Geophysical Research*, *86*(B4), 2593–2644. https://doi.org/10.1029/JB086iB04p02593

Pallister, J. S., & Knight, R. J. (1981). Rare Earth element geochemistry of the Samail ophiolite near Ibra, Oman. *Journal of Geophysical Research*, *86*, 2673–2697. Retrieved from <Go to ISI>://A1981LN10300011. https://doi.org/10.1029/jb086ib04p02673

Pearce, J. A., Alabaster, T., Shelton, A., & Searle, M. P. (1981). The Oman ophiolite as a Cretaceous arc-basin complex: Evidence and implications. *Philosophical Transactions of the Royal Society of London - Series A: Mathematical and Physical Sciences*, *300*(1454), 299–317.

Peters, T., Blechschmidt, I., Krystyn, L., Dumitrica, P., Mercolli, I., El Amin, O., & Al Towaya, A. (2005). *Geological map of Ibra (1:100,000)*. Sultanate of Oman, Ministry of Commerce and Industry. Sheet NF 40-48 A.

Phipps Morgan, J. P., & Chen, Y. J. (1993). The genesis of oceanic-crust – Magma injection, hydrothermal circulation, and crustal flow. *Journal of Geophysical Research: Solid Earth*, *98*(B4), 6283–6297. https://doi.org/10.1029/92jb02650

Quick, J. E., & Denlinger, R. P. (1993). Ductile deformation and the origin of layered gabbro in ophiolites. *Journal of Geophysical Research*, *98*(B8), 14015–14027. https://doi.org/10.1029/93jb00698

Rioux, M., Bowring, S., Kelemen, P., Gordon, S., Dudas, F., & Miller, R. (2012). Rapid crustal accretion and magma assimilation in the Oman-UAE ophiolite: High precision U-Pb zircon geochronology of the gabbroic crust. *Journal of Geophysical Research: Solid Earth*, *117*. https://doi.org/10.1029/2012jb009273

Rioux, M., Bowring, S., Kelemen, P., Gordon, S., Miller, R., & Dudas, F. (2013). Tectonic development of the Samail ophiolite: High-precision U-Pb zircon geochronology and Sm-Nd isotopic constraints on crustal growth and emplacement. *Journal of Geophysical Research: Solid Earth*, *118*(5), 2085–2101. https://doi.org/10.1002/jgrb.50139

Shervais, J. W. (2001). Birth, death, and resurrection: The life cycle of suprasubduction zone ophiolites. *Geochemistry, Geophysics, Geosystems*, *2*, 2000GC000080. https://doi.org/10.1029/2000gc000080

Stoll, B., Jochum, K. P., Herwig, K., Amini, M., Flanz, M., Kreuzburg, B., et al. (2008). An automated iridium-strip heater for LA-ICP-MS bulk analysis of geological samples. *Geostandards and Geoanalytical Research*, *32*(1), 5–26. https://doi.org/10.1111/j.1751-908x.2007.00871.x

Sun, S. S., & McDonough, W. F. (1989). Chemical and isotopic systematics of oceanic basalts: Implications for mantle composition and processes. In A. D. Saunders, & M. J. Norry (Eds.), *Magmatism in the ocean basins* (pp. 313–345). Geol. Soc. Spec. Publ. 42. Blackwell. https://doi.org/10.1144/gsl.sp.1989.042.01.19

Teagle, D. A., Ildefonse, B., & Blum, P. (2012). IODP expedition 335: Deep sampling in ODP hole 1256D. *Proceedings IODP*, *335*. https://doi.org/10.2204/iodp.proc.335.101.2012

Tilton, G. R., Hopson, C. A., & Wright, J. E. (1981). Uranium-lead isotopic ages of the Samail Ophiolite, Oman, with applications to Tethyan ocean ridge tectonics. *Journal of Geophysical Research*, *86*(B4), 2763–2775. https://doi.org/10.1029/JB086iB04p02763

VanTongeren, J. A., Kelemen, P. B., Garrido, C. J., Godard, M., Hanghoj, K., Braun, M., & Pearce, J. A. (2021). The composition of the lower oceanic crust in the Wadi Khafifah section of the southern Samail (Oman) ophiolite. *Journal of Geophysical Research: Solid Earth*, *126*(11), e2021JB021986. https://doi.org/10.1029/2021JB021986

VanTongeren, J. A., Kelemen, P. B., & Hanghøj, K. (2008). Cooling rates in the lower crust of the Oman ophiolite: Ca in olivine, revisited. *Earth and Planetary Science Letters*, *267*(1–2), 69–82. https://doi.org/10.1016/j.epsl.2007.11.034

White, W. M., & Klein, E. M. (2014). Composition of the oceanic crust. In H. D. Holland, & K. K. Turekian (Eds.), *Treatise on geochemistry* (2nd ed., pp. 497–541). Oxford: Elsevier. https://doi.org/10.1016/B978-0-08-095975-7.00315-6

Wilson, D. S., Teagle, D. A. H., Alt, J. C., Banerjee, N. R., Umino, S., Miyashita, S., et al. (2006). Drilling to gabbro in intact ocean crust. *Science*, *312*, 1016–1020. Retrieved from http://www.sciencemag.org/cgi/content/abstract/1126090v1. https://doi.org/10.1126/science.1126090

Yamasaki, T., Maeda, J., & Mizuta, T. (2006). Geochemical evidence in clinopyroxenes from gabbroic sequence for two distinct magmatisms in the Oman ophiolite. *Earth and Planetary Science Letters*, *251*, 52–65. https://doi.org/10.1016/j.epsl.2006.08.027

Zihlmann, B., Müller, S., Coggon, R. M., Koepke, J., Garbe-Schönberg, D., & Teagle, D. A. H. (2018). Hydrothermal fault zones in the lower oceanic crust: An example from Wadi Gideah, Samail ophiolite, Oman. *Lithos*, *323*, 103–124. https://doi.org/10.1016/j.lithos.2018.09.008